Structural study of ^{105}Sn using the one-neutron knock-out reaction

A Dissertation Presented for the

Doctor of Philosophy

Degree

The University of Tennessee, Knoxville

Anna Peter

May 2026

© by Anna Peter, 2026
All Rights Reserved.

Dedicated to my family

Acknowledgments

I am grateful to the Almighty, the Most Beneficent and Most Merciful, for His blessings upon me.

I express my heartfelt gratitude to my advisor, Dr. Kate Jones, for her continuous and unconditional guidance, support, and encouragement throughout the course of this research. Her insights, patience, and constructive feedback have been invaluable in shaping this work. I am also deeply grateful to her for providing me with opportunities to attend various workshops, conferences, and experiments, which significantly broadened my knowledge and experience in the field.

I express my sincere gratitude to Dr. Tim Gray, whose wisdom, advice, and insightful suggestions have been integral to the completion of this thesis. I am immensely grateful for his time and effort in introducing me to the fundamentals of nuclear data analysis, as well as advanced data analysis techniques and simulations. His mentorship has also played a significant role in improving my programming skills.

I am also deeply thankful to my committee members, Dr. Robert Grzywacz, Dr. Thomas Papenbrock, and Dr. Jason Hayward, for their time, thoughtful suggestions, and valuable feedback.

I extend my appreciation to my groupmates Ashwin Nagarajan and Amber Stinson and my former group members Dr. Alicia Palmisano, Dr. Jerome Kovoor, and Dr. Rajesh Ghimire for their support, helpful discussions, and the collaborative environment at various stages of my graduate research. I would also like to thank all the collaborators from

different institutions, especially staff and faculty from FRIB, who have helped make this experiment possible by helping with the setup and experiment shifts.

My heartfelt thanks go to my friends, Dony Varghese, Swathy Krishna, Manu Sajeev, and all other friends from Knoxville Malayali Community, for their encouragement and understanding during this journey and for the help during my life in Knoxville. Their support has been a constant source of motivation.

Finally, I am profoundly grateful to my family, my parents. Mr. Peter P. D., Ms. Roseland Peter, who believed in me and supported me throughout every decision I have taken and encouraged me in every stage of life. All my appreciation and love to my husband, Jopaul Mathew, for believing in me when I doubted myself and for being the source of confidence and inner strength that enabled me to undertake this significant journey. I also thank my siblings, all my relatives, and friends for their unwavering love and support. I am deeply humbled by the support and assistance I have received from those around me during this process.

Abstract

There is significant interest in ^{100}Sn owing to its status as the heaviest doubly magic, N = Z nucleus, its location at the end of the rp-process, and its proximity to the proton drip line. However, there is a lack of information on the single particle states for nuclei near ^{100}Sn. In the nuclear shell model, the low-lying neutron orbitals above ^{100}Sn are the $2d_{5/2}$ and $1g_{7/2}$, but their ordering remains an open question. Thus, determination of spin and parity for the lowest states in the proton-rich odd-A Sn isotopes is vital for understanding the region.

In this work, a one-neutron knockout reaction was performed on a ^{106}Sn beam to investigate the single-particle states in ^{105}Sn. The experiment was carried out at the Facility for Rare Isotope Beams (FRIB), using the S800 spectrograph for reaction residue identification and momentum measurements, in conjunction with the GRETINA array for in-beam γ-ray spectroscopy. Exclusive longitudinal momentum distributions were extracted and compared with theoretical expectations to determine the spin and parity of the ground and first excited states. The lifetime of the first excited state was determined from the Doppler-shifted γ-ray lineshape. Exclusive cross-sections for the ground and first excited states were measured and provide some insight into the purity of the nuclear wavefunctions. This experiment, which was performed during the first year of FRIB operations, included neutron knockout measurements on ^{104}Sn, to study low-lying states in ^{103}Sn. The ultimate goal of this program is to gain insights into the single-particle nature of ^{101}Sn, through a future knockout experiment on ^{102}Sn.

Table of Contents

1 Introduction **1**

1.1 Previous studies on light tin isotopes 2

2 Theoretical background **9**

2.1 Nuclear Shell Model 9

2.1.1 Independent particle model 9

2.1.2 Configuration interaction shell model 14

2.2 Knock-out reactions 15

2.3 Spectator Core Eikonal Reaction Model 16

3 Experimental setup **19**

3.1 Primary beam Production 19

3.2 ARIS fragment separator 21

3.3 S800 Spectrograph 23

3.3.1 S800 Focal Plane 26

3.4 GRETINA 32

4 Analysis **34**

4.1 Ionization Chamber calibration: Gain Match 35

4.2 Cathode Readout Drift Chamber calibration: Mask Calibration 35

4.3 Ionization chamber calibration: Position Correction 40

4.4 Time of Flight correction 40

4.5 GRETINA Analysis . . . 41
4.5.1 Doppler Correction . . . 41
4.6 GEANT4-UCGretina Simulation . . . 50
4.6.1 FitGretina . . . 52
4.6.2 Lifetime measurements . . . 53
4.7 Momentum Distribution Calculations . . . 55
4.7.1 Extracting momentum distributions for excited states . . . 58
4.8 Cross Section Calculations . . . 59

5 Results and Discussion **62**
5.1 Identification of reaction channels . . . 62
5.1.1 Particle identification spectra . . . 62
5.2 γ-ray Spectra . . . 68
5.3 Lifetime and Spin assignments of first excited state . . . 71
5.4 Momentum distribution for the ground state of ^{105}Sn . . . 72
5.5 Cross Section . . . 75

6 Conclusion **77**
6.1 Future outlook . . . 78

Bibliography **79**

Vita **85**

List of Tables

4.1 Summary table of beam settings before target and reaction settings after target. 50

5.1 Summary table of shell-model spectroscopic factor (C^2S) calculations from ^{106}Sn beam. The experimental calculations for S(J^π) = ($C^2S/(2J+1)$) are compared with the calculations using the jj55pna model space. For jj555pna standard model space $\Delta\varepsilon_{s.p} = 172$keV and for jj55pna(inv) model $\Delta\varepsilon_{s.p} = -172$keV. 75

5.2 Summary table of inclusive and exclusive neutron removal cross sections from ^{106}Sn beam from both experimental and theoretical calculations. The inclusive cross section is the total cross section of the reaction, regardless of the knockout channel. 76

5.3 Summary of relative cross sections calculated ($\sigma(7/2^+)/\sigma(5/2^+)$) from the experiment and the two model spaces: jj55pna and jj55pna(inv). 76

List of Figures

1.1 Spectrum of γ rays correlated with decay events associated with ^{101}Sn β-delayed protons protons [1]. 5

1.2 Top: Proposed α decay chain ^{109}Xe $\rightarrow$ ^{105}Te $\rightarrow$ ^{101}Sn. Bottom: α decay chain ^{111}Xe $\rightarrow$ ^{107}Te $\rightarrow$ ^{103}Sn [2] 6

1.3 The energy splitting between the $7/2^+$ and $5/2^+$ states in light tin isotopes, obtained from shell-model calculations. Results of shell-model calculations in variants V1 (blue for the N3LO and red for the AV18 residual interactions) and V2 (green) for the splitting of the $7/2^+$ - $5/2^+$ states in the neutron-deficient, odd-mass tin isotopes adapted from [2]. . . . 7

1.4 Momentum distribution of the ^{107}Sn reaction residue in the first excited state following the one-neutron knockout from ^{108}Sn. The data overlaid to eikonal model reaction calculations for neutron removal from a $2d_{5/2}$ orbital (blue solid) and a $1g_{7/2}$ orbital (red dashed) adapted from [3]. 8

2.1 Schematic diagram of shell model single particle energies. The degeneracy splitting from the spin-orbit interaction is indicated. The final orbitals are denoted in the order *nlj* notation, where *n* is the principal quantum number, *l* the orbital angular momentum (s, p, d, f, g, etc) and *j* the total angular momentum of the orbital. The magic numbers are the total number of nucleons required for a closed shell adapted from [4]. 12

2.2 Different potentials as a function of radius. The square well is V_{sq} , harmonic oscillator is V_{ho} and Woods-Saxon potential is V_{WS} adapted from [5]. 13
2.3 One-nucleon knockout schematic adapted from [5]. 15
2.4 Momentum distribution of the ^{14}C reaction residue in the ground state (circles) following the one-neutron knockout from ^{15}C and in coincidence with the gamma ray (triangles). The data overlaid to eikonal model reaction calculations for neutron removal (dashed is the ground state and dot-dashed is the 1^- state) adapted from [6]. 18

3.1 Layout of the FRIB facility [7]. 20
3.2 Design of the Advanced Rare Isotope Separator (ARIS) at FRIB [8]. 22
3.3 A schematic of the S800 spectrograph [9]. 24
3.4 (a) Focus mode of operation of the analysis line. The maximum dispersion (angular) is reached at the intermediate image plane. (b) Dispersion-matching mode of operation of the analysis line. Image source : https://wikihost.nscl.msu.edu/S800Doc/doku.php/id=modes_of_operation 25
3.5 A schematic of the S800 Spectrograph Focal Plane. Image source: https://wikihost.nscl.msu.edu/S800Doc/lib/exe/detail.php?id=detectors&media=wiki:s800_fp_detectors.jpg 26
3.6 A schematic view of CRDC. Image source: https://wikihost.nscl.msu.edu/S800Doc/doku.php/id=detectors/ionization_chamber . . 27
3.7 The principle of operation of a CRDC. Image source: https://wikihost.nscl.msu.edu/S800Doc/doku.php/id=detectors/ionization_chamber 29
3.8 Ionization Chamber. Image source: https://wikihost.nscl.msu.edu/S800Doc/doku.phpid=detectors_ionization_chamber 31

3.9 A "beam-view" shot (from the upstream looking towards the S800 Spectrograph). Image source: https://people.nscl.msu.edu/noji/gret12det 33

4.1 The energy loss signal in each ion chamber must be matched. Plots of the uncalibrated (a) and the calibrated (b) energy loss measurements are shown for each channel of the ionization chamber. Channel 7 was not working. . . 36

4.2 (a) The mask pattern used for the calibration from https://wikihost.nscl.msu.edu/S800Doc/lib/exe/fetch.php/media=wiki:mask.pdf. (b) The X versus Y positions recorded by the first CRDC are plotted for a mask calibration run. The mask pattern is clearly visible. 37

4.3 Ionization chamber energy loss as a function of dispersive position (x) and angle (a_{fp}) at CRDC1. Panels (a,b) show uncorrected and corrected spectra versus dispersive position, while (c,d) show the corresponding spectra versus dispersive angle. 38

4.4 Energy loss as a function of non-dispersive position (y) and angle (b_{fp}) at CRDC1. Panels (a,b) show uncorrected and corrected spectra versus position y, while (c,d) show the corresponding spectra versus angle b_{fp}. . . 39

4.5 The TOF is plotted with respect to the x (dispersive) position of the particles. The uncorrected spectrum (a) indicates that the TOF varies greatly depending on the position. This spread causes the TOF of the isotopes to overlap. The corrected (b) shows the result after adjusting the TOF for the position of the particle. 42

4.6 The TOF is plotted with respect to the y (non-dispersive) position of the particles. The uncorrected spectrum (a) and the corrected spectrum (b) . . . 43

4.7 The TOF is plotted with respect to their trajectory angle (a_{fp}) in the dispersive position of the particles. In the uncorrected (a) spectrum, it is impossible to distinguish between the isotopes. The corrected (b) spectrum shows them much more clearly. 44

4.8 The TOF is plotted with respect to their trajectory angle (b_{fp}) in the non-dispersive position of the particles. The uncorrected (a) and corrected spectrum (b). 45
4.9 Schematic diagram illustrating the geometry used for Doppler correction of emitted γ rays. The emitted γ ray is detected at an angle θ with respect to the fragment velocity vector 46
4.10 The figure shows the level scheme of ^{105}Sn as taken from the ENSDF [10]. The energies of the levels, together with their half-lives, are shown on the right, while spin-parity for levels is shown on the left. The energy of transitions is represented by transition arrows. The energies are in keV. . 47
4.11 The x-axis represents detected gamma ray energy (keV), whereas the y-axis represents the measured gamma ray emission angle (in degrees). The vertical structures indicate gamma rays from neutron-induced events in stationary backgrounds, whereas the slanted lines represent transition gamma rays. 48
4.12 The gamma ray spectrum for ^{105}Sn before (a) and after (b) applying Doppler corrections. The top spectrum presents laboratory frame gamma spectra with peaks corresponding to numerous background neutron-induced reactions, whereas the bottom spectrum shows how these peaks disappear after Doppler shift correction and the knockout reaction peaks become visible. 49
4.13 Simulated response functions for excited states 200 kev, 1194 keV, 1394 keV and 1849 keV. 51
4.14 A short-lived state gives narrow peak and long-lived state results in broadened peak 54

4.15 χ^2 fitting for the simulated half-life and uncertainty determined from the one-standard-deviation confidence interval. The blue points represent the χ^2 values from the simulations for different half-life values shown on the x-axis. The red curve is the quadratic fit to the χ^2 distribution. The horizontal dashed line indicates the $\chi^2_{\text{min}} + 1$ level, which defines the uncertainty limits on the half-life. The green shaded region represents the previously reported half-life from the work [11], and the orange shaded region is the half-life range obtained in the present work. 56

5.1 The unreacted beam incoming PID for one run. The TOF from the E1-OBJ scintillator is plotted against the TOF from the E1-XFP scintillator. The $N = 56$ isotones contaminants were present in the secondary incoming beam. 64

5.2 The reacted incoming PID from all the reaction settings data runs . The TOF from the E1-OBJ scintillators is plotted against the TOF from the E1-XFP scintillator. The ^{106}Sn incoming beam gate allows to select all the reaction products from that beam. 65

5.3 Energy loss in the S800 ionization chamber as a function of time-of-flight between the E1 and OBJ scintillators before corrections are applied. (a) shows the PID with no corrections and gamma gate applied, (b) shows the PID with the first-order ionization chamber and scintillator corrections. . . 66

5.4 Energy loss in the S800 ionization chamber as a function of time-of-flight between the E1 and OBJ scintillator after applying calibrations and corrections to S800 focal plane detectors with a γ-ray coincidence requirement. Each of the different blobs represents a single isotope. While the vertical structure correlates to comparable A/q ratios, each nearly horizontal line represents a specific element. Each blob can have gates drawn around it for data processing of the gamma rays detected by GRETINA and ^{105}Sn gate used for further analysis is marked. The inset is zoomed into the tin isotopes. 67

5.5 The Doppler-corrected gamma ray spectrum following the one-neutron knockout reaction on ^{106}Sn beam. Simulated spectra for states populated resulting the γ-ray transitions are plotted on the x-axis, with total fitting given as red line using the Maximum Likelihood method. The neutron background for the fitting is given as a green line. The fit also takes into account an exponential background. 69

5.6 The spectra are separated into those where more than one γ-ray was detected ($\gamma_{\text{mul}} > 1$)(blue shaded region) and those where only one gamma ray was detected ($\gamma_{\text{mul}} = 1$)(green shaded region) and fitted using the UCGretina framework. The peak-to-background is much larger for $\gamma_{\text{mul}} = 1$, especially at low energies. 70

5.7 The momentum distribution of ^{105}Sn reaction residue in the first excited state compared with the eikonal model calculations for neutron removal from $l = 2$ (green), and $l = 4$ (red) orbitals. Data is fitted for the shaded region. The χ^2 value for both fit are $\chi^2 = 9.54$ and 194 for $l = 4$ and $l = 2$ fits, respectively. Hence $l = 4$ gives a good fit for the momentum distribution for the first excited state. 72

5.8 The inclusive momentum distribution for ^{105}Sn reaction residue (black points), with momentum distributions for the four lowest excited states scaled by the factor from simulated events. 73

5.9 The exclusive momentum distribution for the ground state of the ^{105}Sn reaction residue is obtained by subtracting the momentum distributions of all dominant bound excited states from the inclusive momentum distribution. The data is overlaid with eikonal model reaction calculations assuming $l = 2$ (red) and $l = 4$ (green) knockout. The χ^2 value for both fit are $\chi^2 = 5.03$ and 48.20 for $l = 2$ and $l = 4$ fits, respectively. Hence $l = 2$ gives a good fit for the momentum distribution for the ground state. The structure seen in the lower momentum region is from the unreacted beam contaminants and hence not taken into account in any calculations. 74

Chapter 1

Introduction

The properties of atomic nuclei are determined by the number of protons and neutrons within the nucleus, and their interactions. For every element present in nature, a number of isotopes exist—nuclei with the same number of protons but different numbers of neutrons. The study of isotopes provides crucial insights into the structure and dynamics of the nucleus. The structure of the atomic nucleus is influenced by the filling of shells with neutrons and protons, analogous to electronic shells in the atom. While the structure of nuclei around stability has been extensively studied, the properties and structure of nuclei far from stability are less well understood due to their short lifetimes and small production cross-sections. ^{100}Sn is an important nucleus, as it is a doubly magic nucleus with completely filled proton and neutron shells at N = Z = 50. This means it is of great interest for studying and testing the shell model. The ^{100}Sn isotope is the heaviest N=Z doubly magic nucleus bound against ground state proton decay. Additionally, the tin nuclei in this region have proximity to the proton drip line and are important for astrophysical calculations [12]. The rapid proton capture process (rp process) proceeds up to the end of the tin isotopic chain, and knowing the properties of the nuclei involved in the rp-process is important to understand the synthesis of proton-rich nuclei as well as X-ray bursts.

Despite the importance of the region, there is a lack of information on the single-particle states in the nuclei outside the doubly magic ^{100}Sn. This work aims to find the

spin and parity of the ground and first excited states in ^{105}Sn, and determine the degree of configuration mixing present in the ground state of ^{106}Sn.

1.1 Previous studies on light tin isotopes

The nuclear shell model predicts that the lowest-lying neutron single-particle states above ^{100}Sn are the $2d_{5/2}$ and $1g_{7/2}$ orbitals. However, the ordering of these orbitals remains an open question. The first study of the single particle states outside the doubly magic core of ^{100}Sn was made by Seweryniak *et al.* [1]. The study shows that the $2d_{5/2}$ and $1g_{7/2}$ orbitals are almost degenerate in ^{101}Sn, separated by only 172 keV[1]. The reaction used to study the energy splitting between the lowest states is the ^{46}Ti(^{58}Ni,3n)^{101}Sn fusion evaporation reaction. In the experiment, detectors were used to detect the in-beam γ rays associated with the production of ^{101}Sn, and assosiated with β-delayed protons from the decay of ^{101}Sn. The γ ray spectrum, shown in Fig. 1.1, has a clearly visible peak at 172 keV, which was interpreted as the transition between the low-lying $7/2^+$ ($g_{7/2}$) and $7/2^+$ ($d_{5/2}$) states. With the help of shell model calculations, the authors interpreted this as a $5/2^+$ ground state, and a low-lying $7/2^+$ first excited state with dominant $d_{5/2}$ and $g_{7/2}$ character, respectively. The spacing and order of these states with the $5/2^+$ state below the $7/2^+$ could be reproduced by a reduction of about 30% in the $(g_{7/2})^2{}_{0+}$ matrix element.

However, a later study by Darby *et al.* [2] concluded that ^{101}Sn has a $7/2^+$ ground state and first excited state with $J^\pi = 5/2^+$. These states were observed through double-α decay chain from ^{109}Xe $\rightarrow$ ^{105}Te $\rightarrow$ ^{101}Sn. Two α decays of 3910(10) keV and 4063(4) keV were observed for the ^{109}Xe $\rightarrow$ ^{105}Te transition, and the ^{105}Te $\rightarrow$ ^{101}Sn transition resulted in two more α decays of 4711(3) keV and 4880(20) keV (see Fig. 1.2). The large α-decay branches for the 3910 keV and 4711 keV decays are interpreted as being due to the zero orbital angular momentum change ($\Delta l = 0$) of the α-decay transition. This compensates for the decreased α-decay energy when compared to the 4063 keV and 4880 keV ground state transitions ($\Delta l = 2$). The difference in the energies gives excitation energies of 153(11) keV for the first excited state in ^{105}Te and 170(20) keV for the first excited state in ^{101}Sn. The

latter value is consistent with the γ ray from the lowest excited state of ^{101}Sn, discussed in Seweryniak *et al.* [1]. The large branching ratio of 89(4)% from the ^{105}Te ground state to the ^{101}Sn first excited state suggests that these two states have the same spin, while the spins of the ground states of ^{105}Te and ^{101}Sn are different. Supported by an alternate shell model calculation [13], the study concluded that the ground state of ^{101}Sn is not $5/2^+$, but $7/2^+$, being dominated by the $g_{7/2}$ neutron single-particle state (see Fig 1.3). This indicates an unexpected level inversion occurring between ^{101}Sn and ^{103}Sn, with the normal ordering being reestablished between ^{109}Sn and ^{111}Sn, as shown in Figure 1.2. They concluded that this inversion is generated by paring correlations due to the close proximity of the $d_{5/2}$ and $g_{7/2}$ orbitals, and this results in highly mixed wavefunctions of the $5/2^+$ and $7/2^+$ states with similar amounts of $d_{5/2}$ and $g_{7/2}$ neutron single particle strength. Thus, firm experimental assignments for the pairs of low-lying states in the odd-A Sn isotopes is imperative to inform our understanding of the region and constrain shell model calculations and degree of mixing.

Intermediate-energy one-nucleon knockout reactions are an excellent tool to study the ordering and nature of single-particle states in the light tin region. Knockout reactions are direct reactions that are sensitive to single-particle structure and angular-momentum transfer. Thus, they can be used to assess both the wavefunction purity/mixing of nuclear states, as well as their l-values for the purposes of spin-parity assignments. With fast beams, viable experiments can be conducted with very low beam rates, due to the ability to use very thick targets. This makes knockout an ideal probe far from stability where intense beams are not available. A study by Cerizza *et al.* [3] is such an experimental study which used a one-neutron knockout reaction on ^{108}Sn. The cross-sections measured are sensitive to the relative contribution to the wavefunction of the $d_{5/2}$ and $g_{7/2}$ orbital. A primary beam of ^{124}Xe at 140 MeV/u from the National Superconducting Cyclotron Laboratory at Michigan State University was used. The secondary beam, separated by the A1900 fragment separator was delivered to the S800 magnetic spectrometer, where the beam impinged on a ^{9}Be target. The target was surrounded by the high-efficiency CsI(Na) scintillator array (CAESAR) which identified the γ rays of the reaction products. The

momentum distributions of the resulting residues reflect the orbital angular momentum (l-value) of the removed neutron, and were used to assign the spin of the ground state as $5/2^+$ and first excited state as $7/2^+$ by comparisons to Eikonal-model reaction calculations [14].

The knockout reaction method is used in this work for extracting the nuclear structure information of ^{105}Sn using low-intensity radioactive ion beams. The aim of this work is to measure one-neutron knockout of ^{106}Sn using GRETINA and the S800 at Facility for Rare Isotope Beams (FRIB), with the goal of establishing the ordering of the $5/2^+$ and $7/2^+$ states in ^{105}Sn. The method also provides a way to study the mixing of the $5/2^+$ and $7/2^+$ states through cross-section measurements.

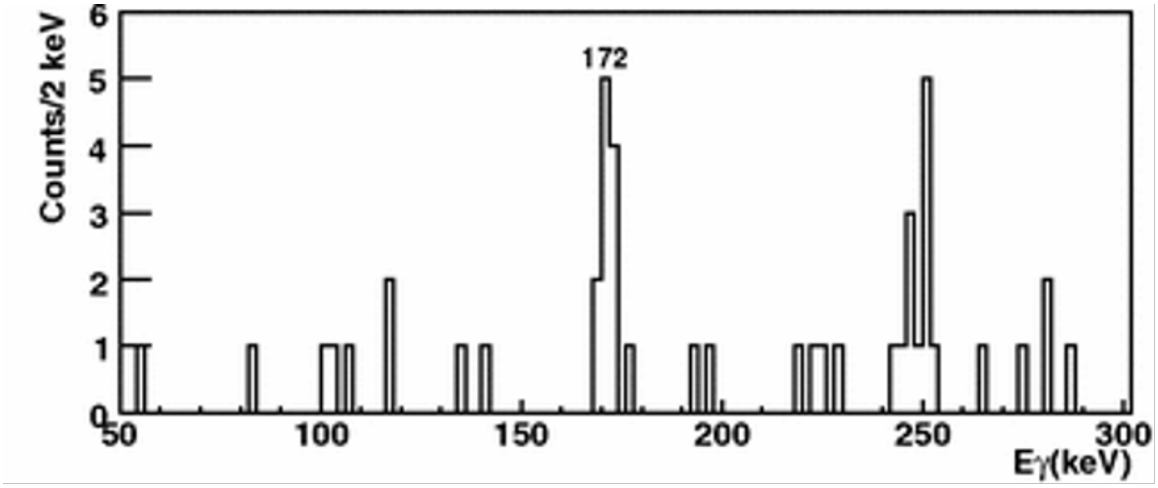


Figure 1.1: Spectrum of γ rays correlated with decay events associated with ^{101}Sn β-delayed protons protons [1].

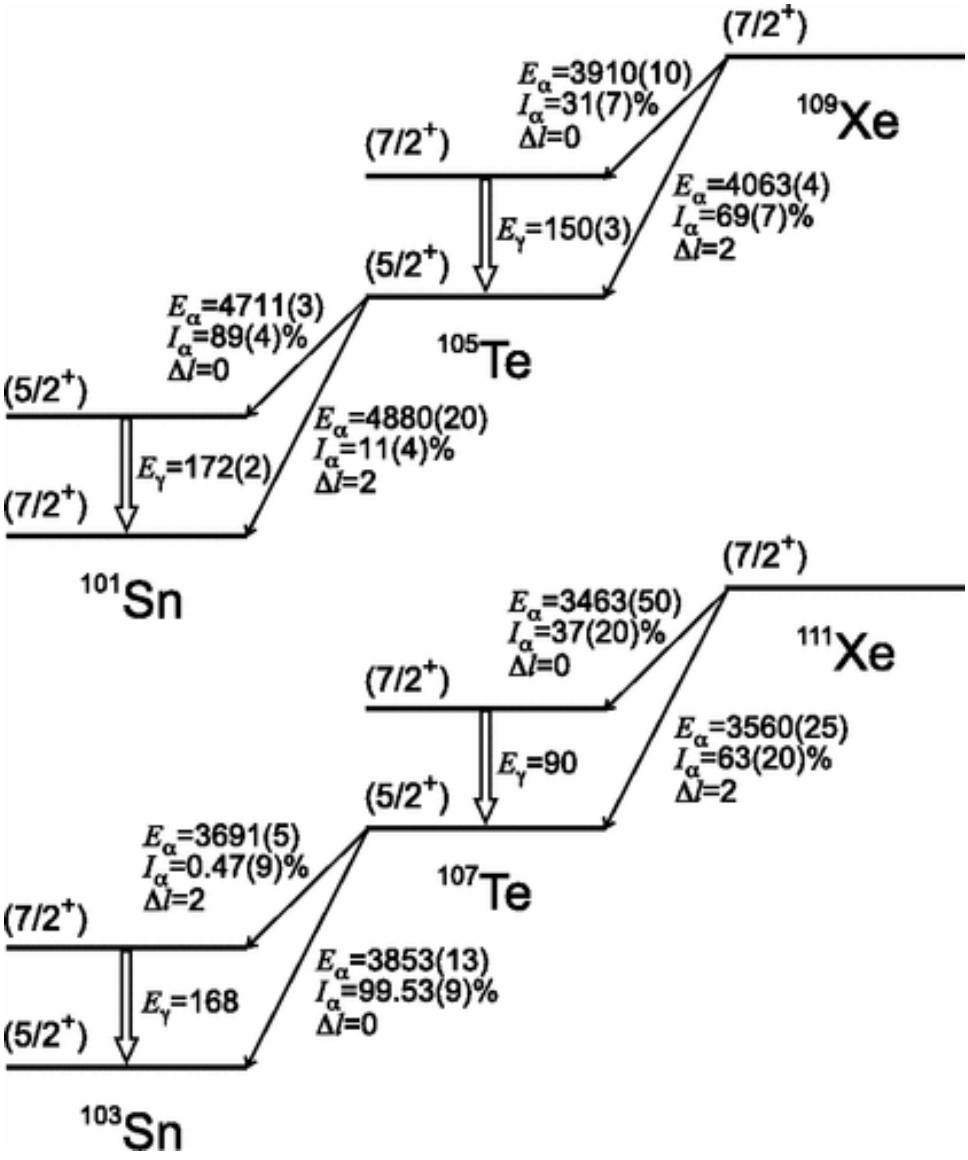


Figure 1.2: Top: Proposed α decay chain ^{109}Xe $\rightarrow$ ^{105}Te $\rightarrow$ ^{101}Sn. Bottom: α decay chain ^{111}Xe $\rightarrow$ ^{107}Te $\rightarrow$ ^{103}Sn [2]

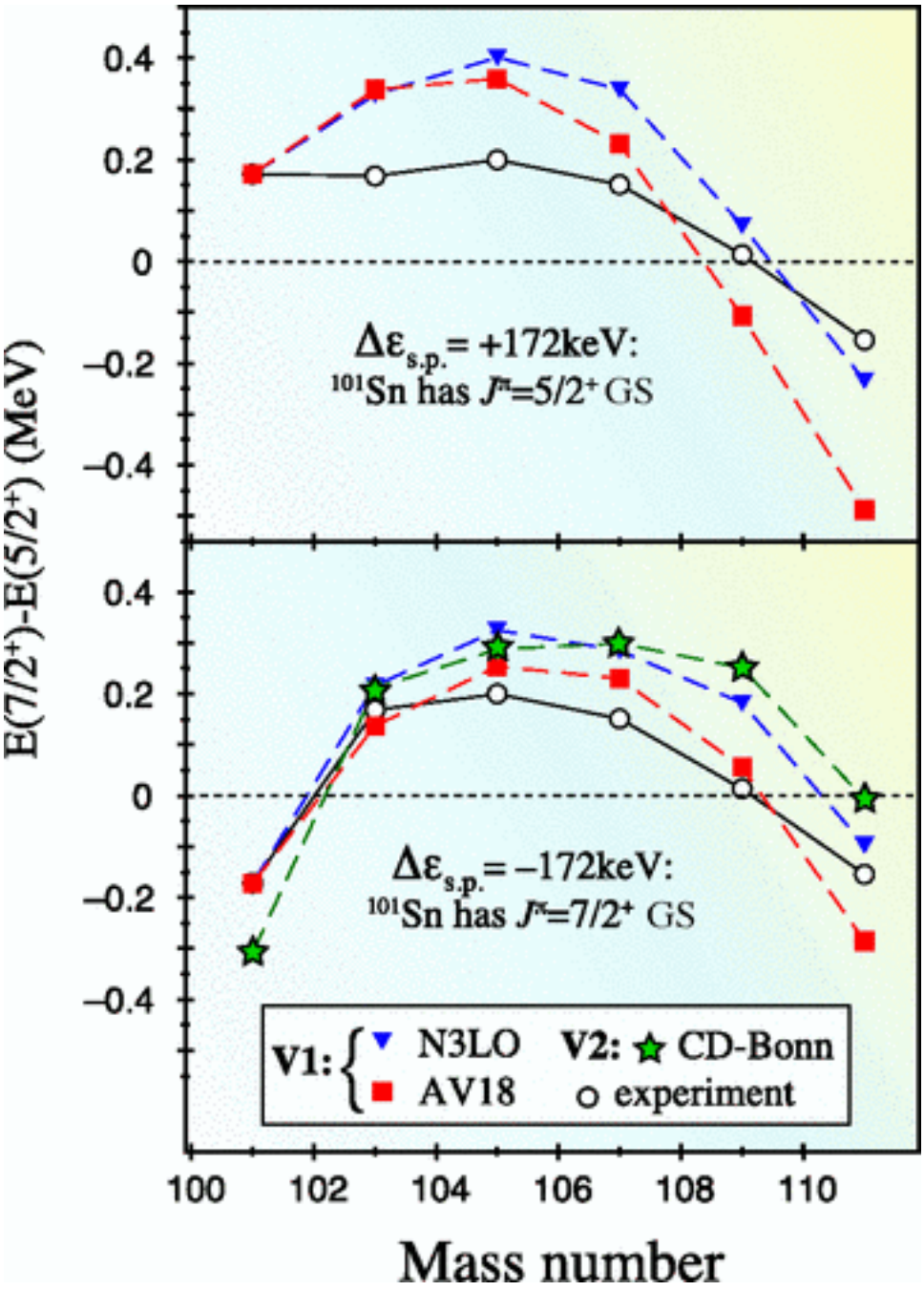


Figure 1.3: The energy splitting between the $7/2^+$ and $5/2^+$ states in light tin isotopes, obtained from shell-model calculations. Results of shell-model calculations in variants V1 (blue for the N3LO and red for the AV18 residual interactions) and V2 (green) for the splitting of the $7/2^+$ - $5/2^+$ states in the neutron-deficient, odd-mass tin isotopes adapted from [2].

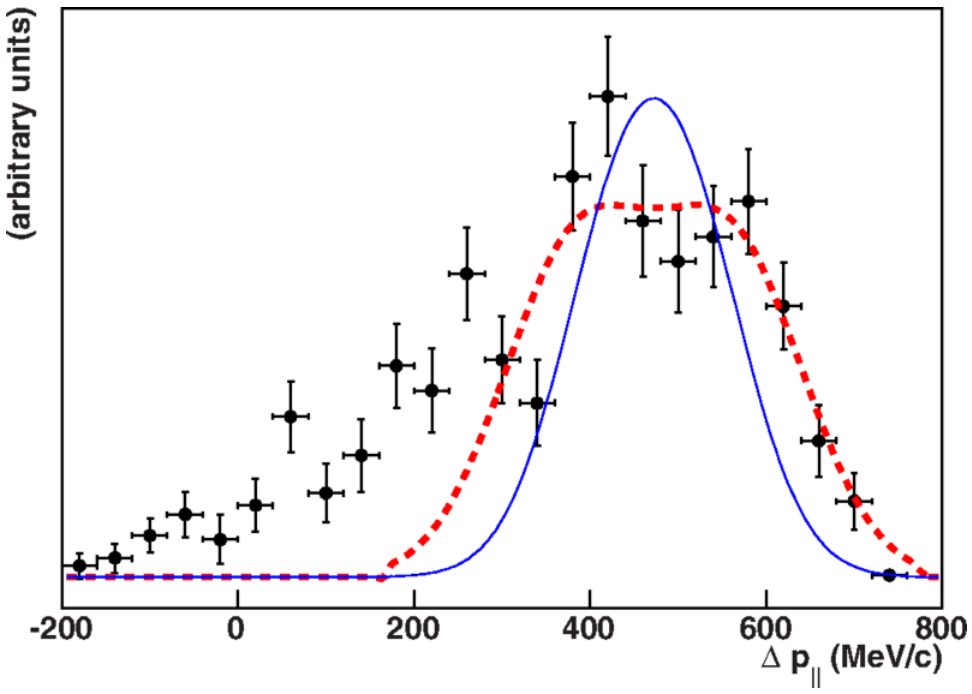


Figure 1.4: Momentum distribution of the ^{107}Sn reaction residue in the first excited state following the one-neutron knockout from ^{108}Sn. The data overlaid to eikonal model reaction calculations for neutron removal from a $2d_{5/2}$ orbital (blue solid) and a $1g_{7/2}$ orbital (red dashed) adapted from [3].

Chapter 2

Theoretical background

2.1 Nuclear Shell Model

The nuclear shell model is a foundational framework in nuclear physics that describes the structure of atomic nuclei in terms of energy levels or "shells", much like the arrangement of electrons in an atom. Developed in the mid-20th century by physicists Maria Goeppert Mayer and J. Hans D. Jensen [15], the model provides a comprehensive explanation for the observed stability of certain nuclei, known as "magic numbers", which correspond to completely filled shells of protons and neutrons. Experimentally, the magic numbers have been determined for stable nuclei to be 2, 8, 20, 28, 50, 82, and 126 (for neutrons). This model has been important in understanding nuclear reactions, decay processes, and nuclear structure.

2.1.1 Independent particle model

The independent particle model describes protons and neutrons as non-interacting independent particles in the orbits of a spherical symmetric mean field potential due to all other nucleons in the nucleus. The resulting orbit energies are mass dependent. The one-body

Hamiltonian used by this model is given by:

$$H = -\frac{\hbar^2}{2\mu}\nabla^2 + V(r). \tag{2.1}$$

Here a nucleus (A,Z) is considered as a single nucleon outside the mean field generated by all other nucleons (A-1,Z). Then the potential confining the single external nucleon could be considered as a three-dimensional harmonic oscillator potential given by:

$$V(r) = \frac{1}{2}\mu\omega_0^2 r^2, \tag{2.2}$$

where μ is the reduced mass of the nucleon, ω_0 is the frequency of the oscillator and r is the radial distance. The reduced mass of the nucleon is the effective mass calculated by the formula

$$\mu = \frac{m_1 m_2}{m_1 + m_2}, \tag{2.3}$$

where m_1 is the mass of the nucleon (either a proton or a neutron) and m_2 is the mass of the remaining nucleus (the nucleus minus the nucleon being considered).

However, the harmonic oscillator potential only produces energy levels that are evenly spaced and hence only reproduces the first three magic numbers but not the later ones (see the left side of the Fig. 2.1). The magic numbers can be obtained by adding a spin-orbit interaction to the central potential [15]. This is the effect due to the interaction of nucleon spin with its motion inside the potential. The spin-orbit interaction depends on the intrinsic spin s and the orbital angular momentum l of the nucleon. The modified single-particle Hamiltonian is given by:

$$H = -\frac{\hbar^2}{2\mu}\nabla^2 + \frac{1}{2}\mu\omega_0^2 r^2 + a(\vec{L}\cdot\vec{S}) + b\vec{L}^2. \tag{2.4}$$

Here a is the parameter that determines the strength of the spin-orbit coupling, which depends on the number of nucleons, and $\vec{L}^2$ part is the centrifugal term associated with the orbital angular momentum which lowers the centroid energy of large l-values states.

The effect of the spin-orbit modification on the degeneracy of the states can be seen in Figure 2.1. This addition to the three-dimensional harmonic oscillator reproduces the experimentally observed magic numbers.

Another realistic potential to reproduce the experimental magic numbers is the Woods-Saxon potential. The harmonic oscillator potential goes to infinity as distance from the center, r, increases. Hence the Woods-Saxon potential is a better approximation to the nuclear mean field, which would approach a constant as r becomes larger than the nuclear radius (see Fig. 2.2).

The Woods-Saxon potential is given by:

$$V(r) = \frac{V_0}{1 + e^{(\frac{r-R}{a})}}, \tag{2.5}$$

where r is the radial distance, V_0 is the depth of the potential, which is of the order of -50 MeV, nuclear radius, $R = 1.27A^{1/3}$, where A is the atomic mass, a is the diffuseness, which has a value generally between 0.6 fm and 0.8 fm. However this still does not reproduce the experimental magic numbers. A spin-orbit coupling factor (given in Equation 2.6) is necessary to reproduce the observed magic numbers.

$$V_{LS}(r) = -\frac{V^{'}(r)}{r}\vec{L}\cdot\vec{S}. \tag{2.6}$$

Here $\vec{L}$ and $\vec{S}$ are angular and spin momentum operators respectively and $V^{'}(r)$ is the coupling strength. Thus the magic numbers that were found experimentally for stable nuclei are successfully reproduced.

The harmonic oscillator potential and the Woods-Saxon potential are applicable to nuclei containing a single nucleon outside the closed shell. When more valence nucleons are taken into account, a residual interaction between the valence nucleons must be included. By including this residual interaction, different shell configurations are mixed, and degeneracy of energy states for the same configuration is broken.

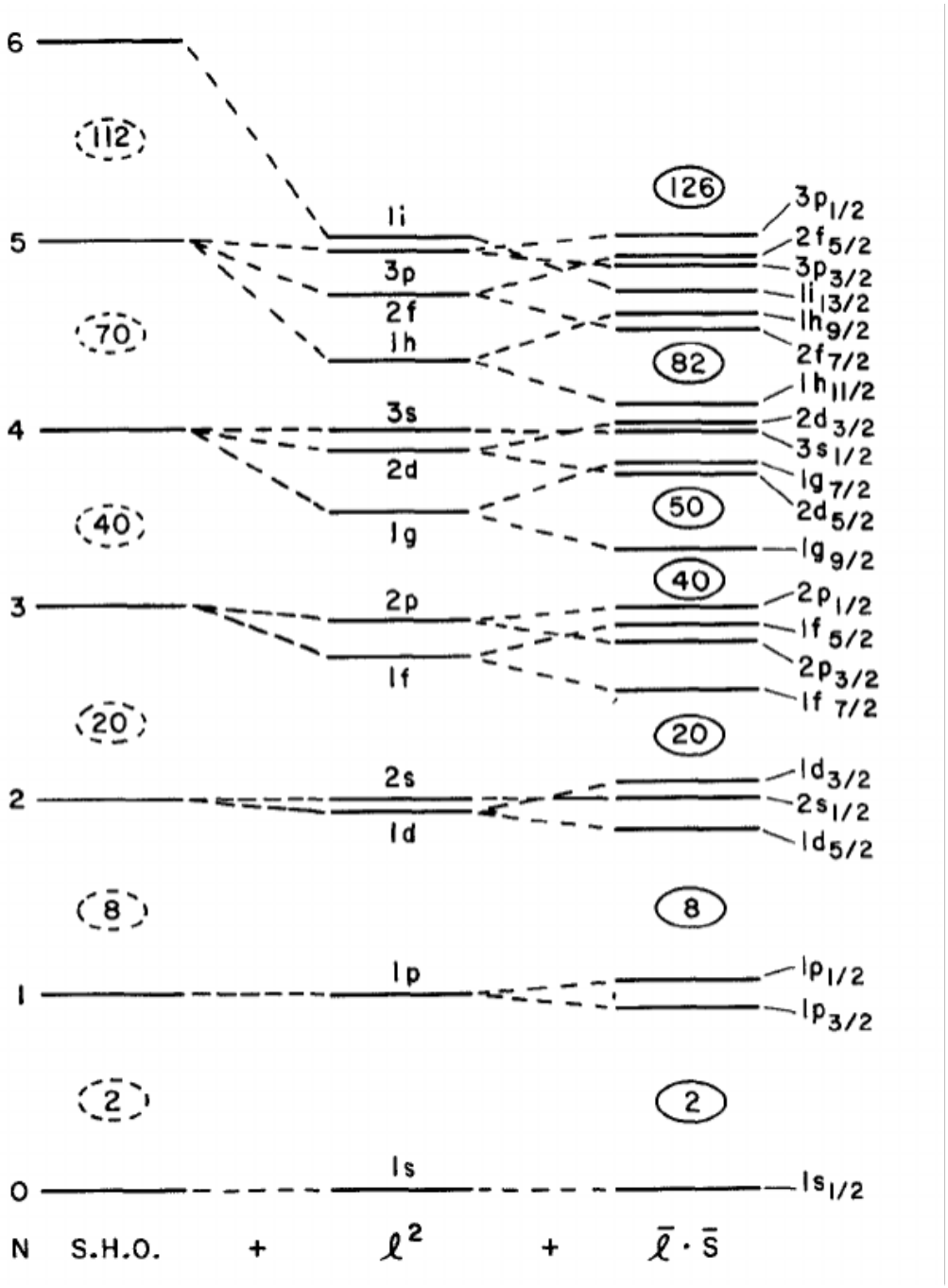


Figure 2.1: Schematic diagram of shell model single particle energies. The degeneracy splitting from the spin-orbit interaction is indicated. The final orbitals are denoted in the order *nlj* notation, where *n* is the principal quantum number, *l* the orbital angular momentum (s, p, d, f, g, etc) and *j* the total angular momentum of the orbital. The magic numbers are the total number of nucleons required for a closed shell adapted from [4].

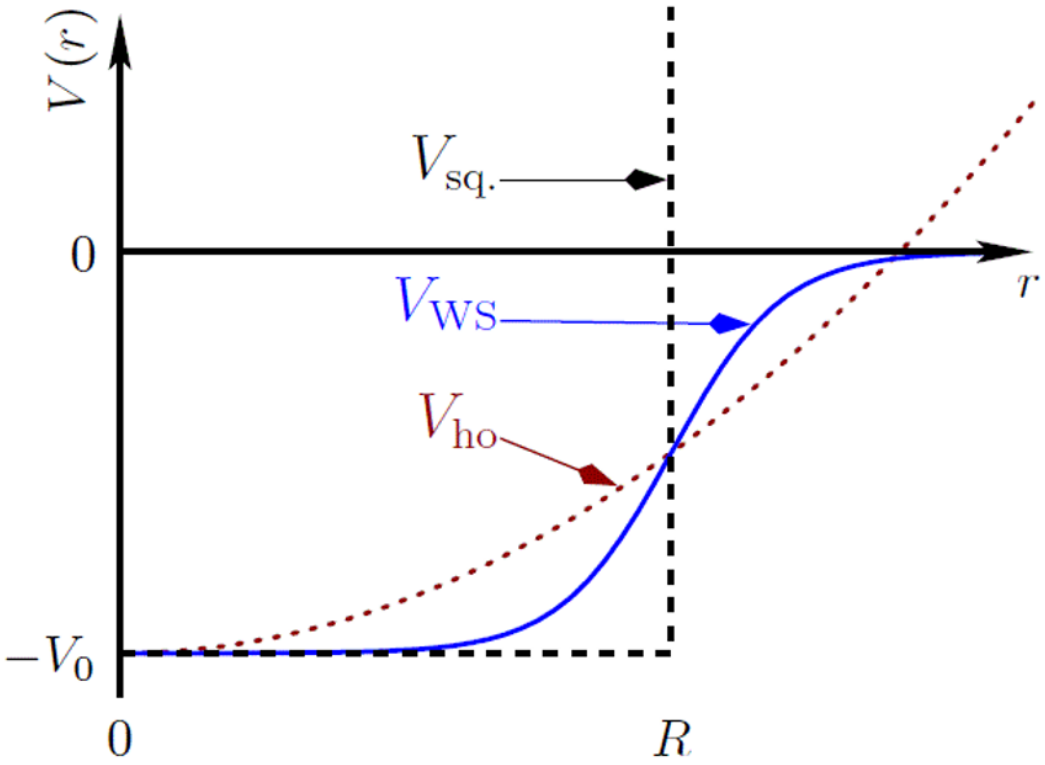


Figure 2.2: Different potentials as a function of radius. The square well is V_{sq} , harmonic oscillator is V_{ho} and Woods-Saxon potential is V_{WS} adapted from [5].

2.1.2 Configuration interaction shell model

Single-particle energies for a simple harmonic oscillator, modified with l^2 and $l \cdot s$ terms gives the potential which reproduces the observed magic numbers (see Fig. 2.1). The Hamiltonian for A nucleons is given by

$$H = T + V = \sum_{k=1}^{A} T(k) + \sum_{1=k<l}^{A} V(k,l), \tag{2.7}$$

where *T(k)* is the kinetic energy and *V(k,l)* is the two-body nucleon-nucleon interaction. It is difficult to find an exact solution for such a many-body problem in higher mass nuclei, as a full calculation with all configurations becomes prohibitively large. This makes truncation necessary. An approximate solution can be obtained by introducing a single particle potential *U(k)* and modifying the Hamiltonian as below:

$$H = \sum_{k=1}^{A} [T(k) + U(k)] + \sum_{1=k<l}^{A} V(k,l) - \sum_{k=1}^{A} U(k) = H^{(0)} + H^{(1)}, \tag{2.8}$$

where $H^{(0)}$ describes an ensemble of independent particles moving in an effective average potential *U(k)* and $H^{(1)}$ corresponds to the residual interactions.

In the interacting shell model approach, the $H^{(0)}$ part of the Hamiltonian is the spherical mean field produced by the closed double magic core (a standard phenomenological single-particle potential given by the harmonic oscillator), and the $H^{(1)}$ part accounts for the configuration mixing between all valence nucleons outside the core [16]. This configuration mixing between valence nucleons interacting through the $H^{(1)}$ part defines the "model space" or "valence space" in which we conduct the calculation. This "valence space" is a number of active shell-model orbits which we allow the nucleons to occupy that are outside the magic core. For isotopes near ^{100}Sn, the orbitals considered will be $2d_{5/2}$, $1g_{7/2}$, $3s_{1/2}$, $2d_{3/2}$ and $1h_{11/2}$ for neutrons, and no valence orbits for protons since Z = 50 is a closed shell. In the valence space, the "interaction" is comprised of both single particle energies (from the $H^{(0)}$ part) and the two-body matrix elements.

The two-body matrix elements define the nucleon-nucleon interactions in the valence space. They determine how each pair of orbits couples to each other pair of orbits for a given angular momentum. There are numerous approaches for determining the two-body matrix elements, including semi-empirically fitting to existing experimental data, as well as *ab initio* methods that begin with microscopic interactions between protons and neutrons.

2.2 Knock-out reactions

Single nucleon knock-out reactions are a powerful tool for nuclear structure studies with fast radioactive ion beams. They can be used to extract the orbital angular momentum l so that the spin and parity of a nuclear state can be determined [17]. A high energy ($\approx$ 100 MeV/nulceon or greater) radioactive beam is impinged on a target to remove an outer nucleon from the projectile nucleus, giving a residue which emerges from the target with nearly the same velocity as the incoming beam (see Fig. 2.3). The momentum of the removed nucleon can be reconstructed from the recoil momentum of the observed heavy residue. Thus, the orbital angular momentum l of the removed nucleon can be obtained from the shape of the longitudinal momentum distribution. The cross sections of the knockout reflect spectroscopic factors, which can be extracted in a model dependent way. These, in turn, can be used to assess the purity of the states populated in the residual nucleus.

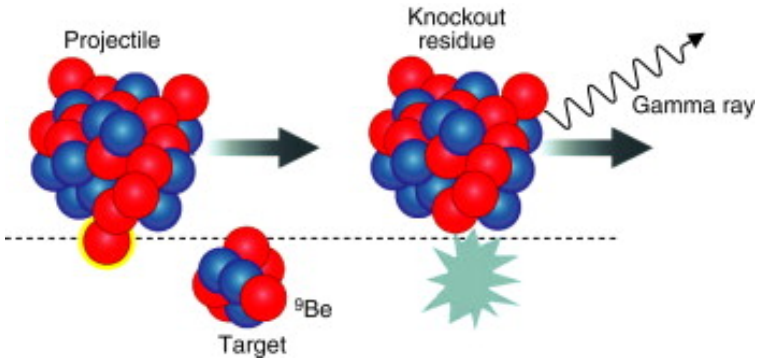


Figure 2.3: One-nucleon knockout schematic adapted from [5].

2.3 Spectator Core Eikonal Reaction Model

The Eikonal reaction model is used to interpret the one-neutron knockout reaction. The reaction is considered as a three-body problem consisting of a target, nucleon, and the core [18]. The core, or knockout residue, is considered as a spectator and is only allowed to interact elastically with the target in the calculation [19]. In one-nucleon knockout reactions, several processes contribute to the total cross section: stripping or inelastic breakup, diffraction or elastic breakup, and elastic breakup due to electromagnetic interaction with the target (Coulomb dissociation) [20]. In light target reactions, like the reaction in this work, the Coulomb dissociation contribution is negligible. Thus, the single particle cross section can therefore be written as

$$\sigma_{\mathrm{sp}} = \sigma_{\mathrm{str}} + \sigma_{\mathrm{diff}} \tag{2.9}$$

The first component, σ_{str}, include all events in which the removed nucleon interacts with the target, leaving it in the excited state. The second component, σ_{diff}, describes the elastic scattering of the nucleon under the two-body interaction with the target, resulting in the nucleon with the forward beam velocity and the target in its ground state.

The eikonal model is based on two approximations: the sudden or fast collision approximation and the eikonal or forward scattering approximation [21]. The sudden approximation assumes that the beam is at a velocity high enough to interact with the target for just a short interval of time, meaning that multi-step processes can be neglected. The eikonal approximation assumes that the trajectory of the projectile after the interaction with the target is considered to be a straight line.

The theoretical inclusive nucleon-removal cross section is given by the sum of the partial cross sections to all bound final states, α, of the residue with excitation energy E^*_α. The formula for the cross section can be written as,

$$\sigma_{\mathrm{th}} = \sum_{\alpha} \left(\frac{A}{A-1} \right)^N C^2 S(\alpha, j^\pi)\, \sigma_{\mathrm{sp}}(j, S^*_\alpha), \tag{2.10}$$

where C^2S is the spectroscopic factor for the removal of a nucleon with (nlj) quantum numbers, $S^*_\alpha = S_{n,p} + E^*_\alpha$ is the effective separation energy for the final state α, and $S_{n,p}$ is the ground-state to ground-state nucleon separation energy. The $N = 2n + l$, is the principal oscillator quantum number of the removed nucleon. For knockout neutrons from a d-shell orbital, $N = 2$.

In order to make spin-parity assignments, the momentum distributions are compared to the momentum distributions calculated from the Eikonal model. If the neutron knocked out from the ^{106}Sn in the reaction is in the $d_{5/2}$ orbital, then a momentum distribution corresponding to a l = 2 neutron knockout will be measured, and if it is in $g_{7/2}$ orbital then a l = 4 neutron knockout will be measured. Examples of such momentum distributions for a ^{14}C reaction residue following one-neutron knockout from ^{15}C in the ground state and in coincidence with the gamma ray in the 1^- state are given in Figure 2.4.

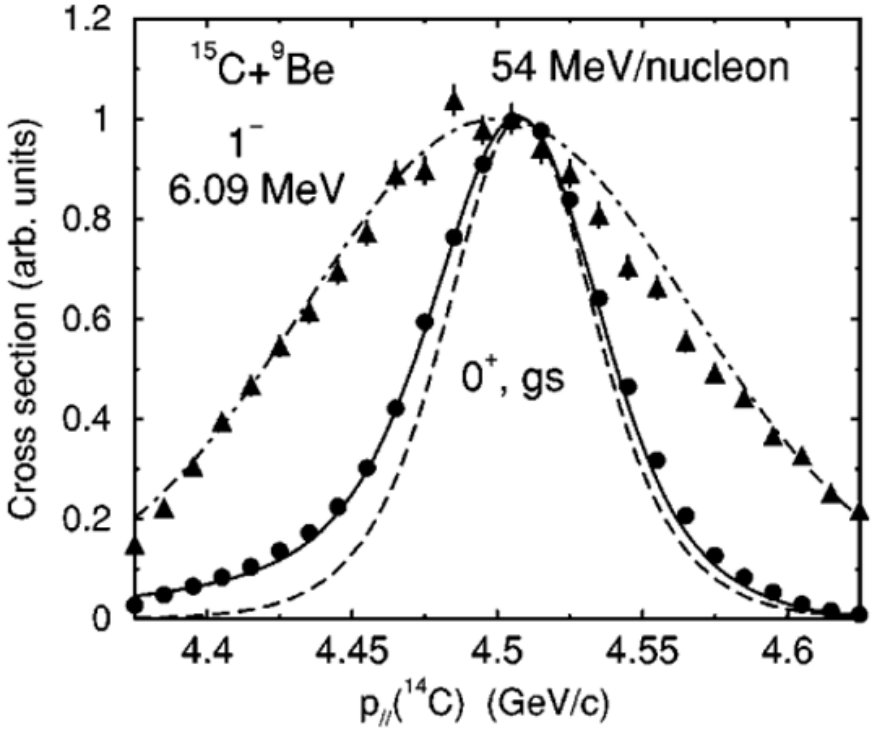


Figure 2.4: Momentum distribution of the ^{14}C reaction residue in the ground state (circles) following the one-neutron knockout from ^{15}C and in coincidence with the gamma ray (triangles). The data overlaid to eikonal model reaction calculations for neutron removal (dashed is the ground state and dot-dashed is the 1^{-} state) adapted from [6].

Chapter 3

Experimental setup

The one-neutron knockout reaction ^{9}Be(^{106}Sn, ^{105}Sn+γ)X was performed at the Facility for Rare Isotope Beams (FRIB) at Michigan State University in December 2022. A primary beam of ^{124}Xe was accelerated in the driver linac (see Fig. 3.1) to 227 MeV/u before being fragmented on a ^{9}Be target. The reaction products were separated using the Advanced Rare Isotope Separator (ARIS), which produced a secondary beam of ^{106}Sn. This beam was directed to a ^{9}Be target in the S800 target chamber. The high-purity germanium detector array, Gamma-Ray Energy Tracking In-Beam Nuclear Array (GRETINA) was used to measure the γ rays that were in coincidence with the knockout reaction. In this chapter, I will present the various stages of the beam production as well as the experimental setup and the techniques used to conduct the ^{9}Be(^{106}Sn, ^{105}Sn+γ)X knockout reaction.

It is useful to define some parameters before proceeding to the subsequent section of information. Particle coordinates x and y represent dispersive and non-dispersive positions, whereas a and b indicate the angle of the particle trajectory in dispersive and non-dispersive directions, respectively. The beam direction is associated with the positive z-axis.

3.1 Primary beam Production

The primary beam used in this experiment was ^{124}Xe at 227 MeV/u from the superconducting (SC) driver linac at FRIB. The front end of the driver linac includes the Superconducting

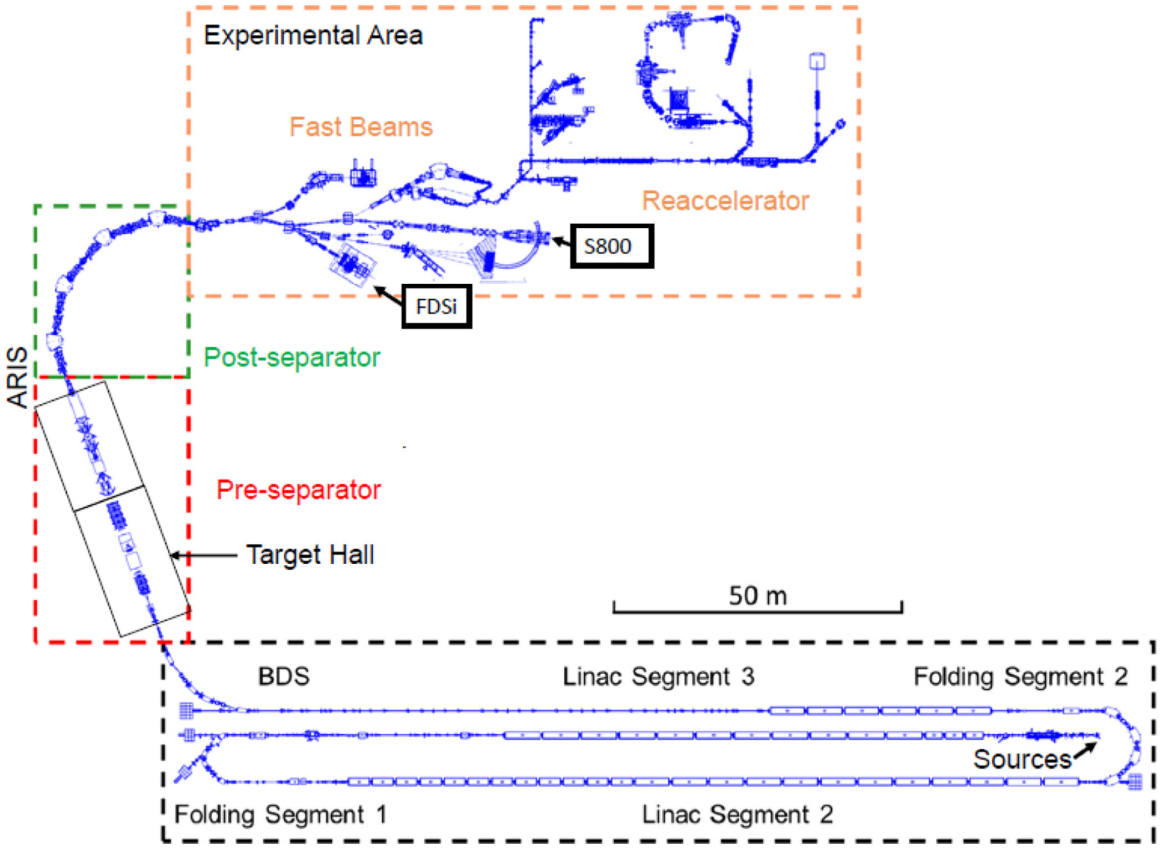


Figure 3.1: Layout of the FRIB facility [7].

Electron Cyclotron Resonance (SCECR) ion sources, a beam bunching system for multi-charge-state beams, and a Radio Frequency Quadrupole (RFQ) [22]. A stable ion beam is generated from either a gas or solid metal by bombardment with electrons. The electrons collide with the material inside the ECR and ionize the atoms. The ionized beam is transported through the Low Energy Beam Transport (LEBT) system and the RFQ to the Medium Energy Beam Transport (MEBT) system, where it transports the beam into SC linac for further acceleration.

The SC linac consist of three segments running parallel to each other, accelerating the primary beam to 227 MeV/u. There are folding segments at the end of each linac segment which bend the beam by 180° before it enters the next segment of linac. The Charge-Stripping Section (CSS) after the first linac segment and before the first bend is used to increase the energy gain of the heavy ion beam by a factor of two [23]. Segment three contains the transverse focusing quadrupoles and beam diagnostics. The beam from the linac is focused on the production target, and the required rare isotope beam is generated in-flight by projectile fragmentation at the production target. The rare isotope beam is then delivered to the fragment separator ARIS.

3.2 ARIS fragment separator

The required radioactive ions are produced by impinging the primary beam on a thick ^{9}Be production target and undergoing projectile fragmentation. The beam collides with the production target nuclei, breaking the beam nucleus and releasing exotic isotopes, which travel with approximately the same velocity as the projectile. The fragment separator is used to separate the nuclear species of interest from the large number of other produced isotopes and the unreacted primary beam.

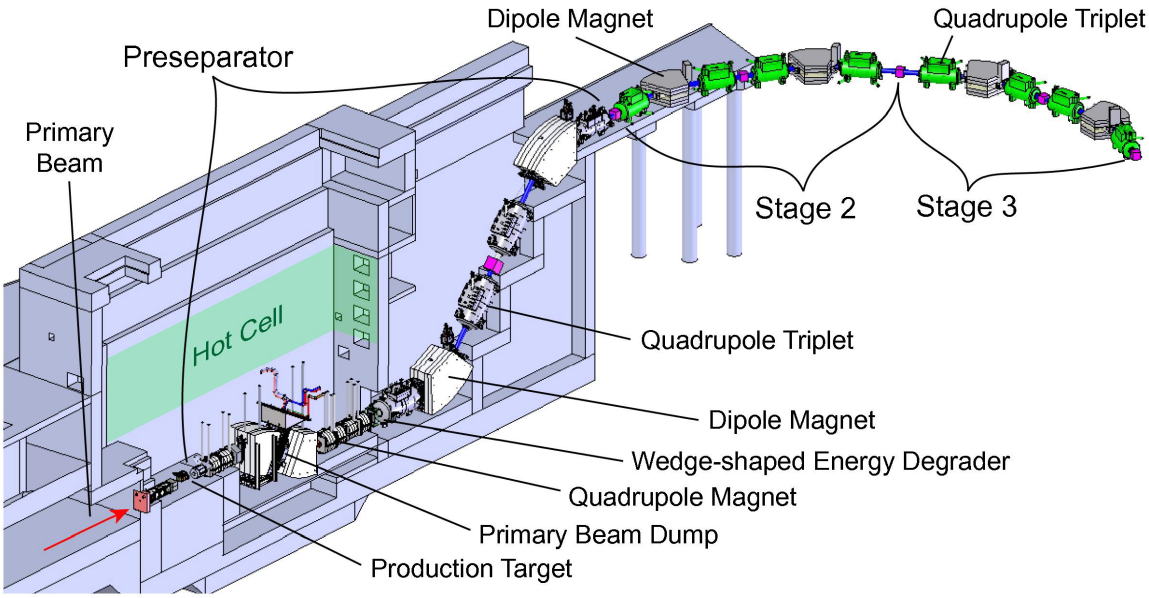


Figure 3.2: Design of the Advanced Rare Isotope Separator (ARIS) at FRIB [8].

The fragment separator used for this experiment is the Advanced Rare Isotope Separator (ARIS) (Fig. 3.2). It consists of three stages [8]. The first stage is the pre-separator that accepts the beam from the production target and performs the first separation of the fragments of interest from other contaminants. It also bends the beam vertically to deliver it to the higher elevation of the second and third stages. To bend the beam and to create the spatial separation needed to separate different beam components, four dipole magnets are used. The second and third stages of the ARIS bend and focus the beam horizontally using the dipole and quadrupole magnets. The four dipole magnets select the desired beam based on its A/q value and eight quadrupole triplets focus the beam either in x or y directions. The operation as two separate stages enables maximum purification of the beam. The ARIS has a maximum magnetic rigidity of 8 Tm.

For this experiment ARIS provided a ^{106}Sn beam with the sufficient beam purity and intensity using its large acceptance and high suppression factor for undesired contaminants. Despite the high suppression factor of ARIS, several significant beam contaminants persisted in the experiment, which will be discussed in Section 5.1.1.

3.3 S800 Spectrograph

The S800 spectrograph is a high-resolution, high angular acceptance spectrograph composed exclusively of superconducting magnets designed for reaction studies with radioactive beams [9]. It has two parts: the analysis line and the spectrograph (see Fig. 3.3). The analysis line begins at the object position and ends at the target station with a total length of 22 m. The spectrograph consists of two quadrupoles, one sextupole, and two dipoles that extend from the target station to the focal plane.

The S800 has two modes of operation: focus mode and dispersion-matching mode. In focus mode, the analysis line is achromatic, and maximum momentum acceptance is achieved, which is $\pm 2\%$. The beam is focused at the target, and the momentum spread of the beam is not canceled at the focal plane (see Fig. 3.4a). The position of the fragment at the focal plane depends on the momentum of the beam upstream of the target. Therefore the

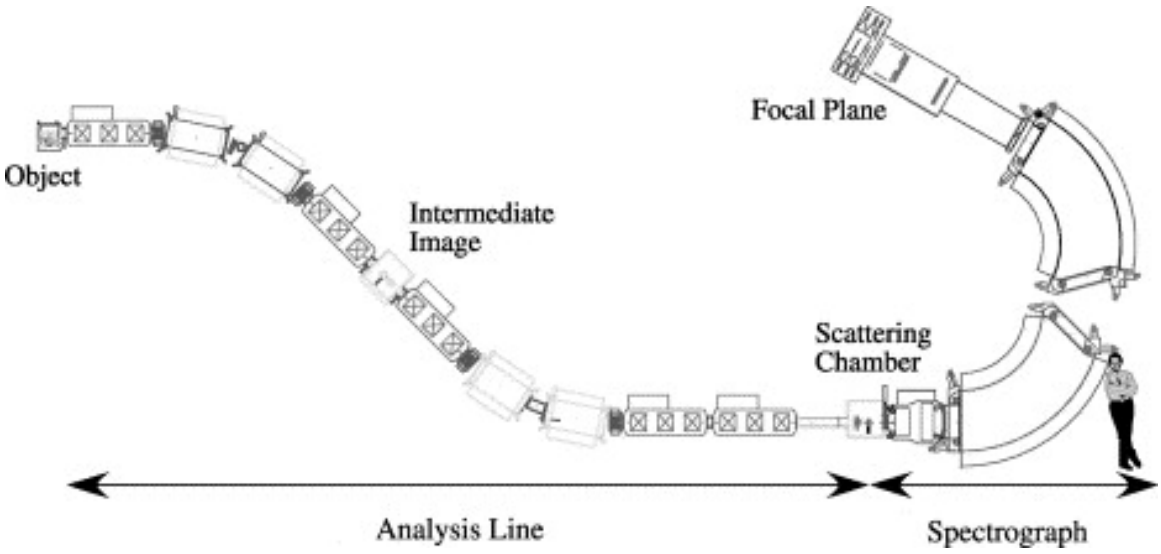
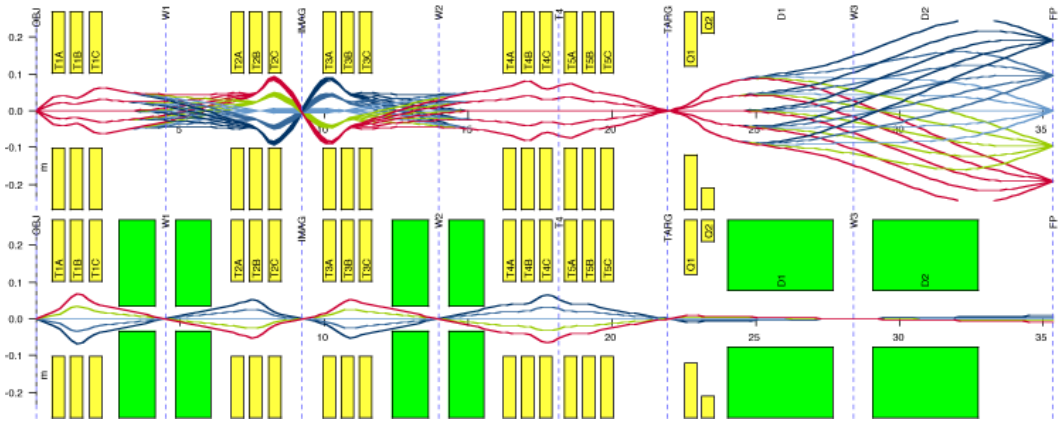


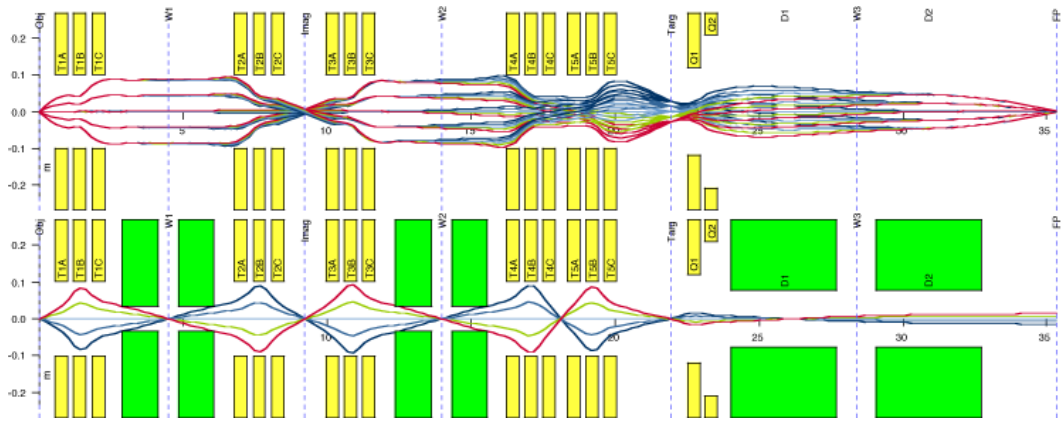
Figure 3.3: A schematic of the S800 spectrograph [9].

momentum of each particle must be tracked to correct for incoming momentum. This limits the energy resolution to about 1 part in 1000 in energy. In dispersion-matching mode, the analysis line is tuned in order to make the whole system (analysis line + spectrograph) achromatic in the focal plane (see Fig. 3.4b). The analysis line is tuned so that the momentum spread of the beam at the object is cancelled at the focal plane. In dispersion-matching mode the highest energy resolution is achieved (1 part in 5000), since momentum tracking is not required. For this experiment we operated in dispersion-matching mode.

A 47 mg/cm^2 thick ^{9}Be target was placed at the target position of the S800. The secondary beam (^{106}Sn) impinged on the target, where, for the reaction channel of interest, a neutron was removed through a direct reaction and a ^{105}Sn residue with nearly the same velocity was formed. The resulting ^{105}Sn residue and residues from other reaction channels with similar A/q ratio, travel through the S800 to its focal plane, which consists of an ionization chamber, two Cathode Readout Drift Chambers (CRDCs), and a plastic timing scintillator. These detectors give energy loss, time of flight, and position measurements used for particle identification.



(a)



(b)

Figure 3.4: (a) Focus mode of operation of the analysis line. The maximum dispersion (angular) is reached at the intermediate image plane. (b) Dispersion-matching mode of operation of the analysis line. Image source : https://wikihost.nscl.msu.edu/S800Doc/doku.php/id=modes_of_operation

3.3.1 S800 Focal Plane

The S800 focal plane is where all the S800 detectors that measure the charge, energy, position, and time of flight of transmission are located. The focal plane is equipped with detectors for particle identification and trajectory reconstruction. The order of the detectors are two Cathode Readout Drift Chambers (CRDCs), followed by the ionization chamber, a thin plastic scintillator (E1 scintillator), and a hodoscope. The hodoscope detector was not used for this work.

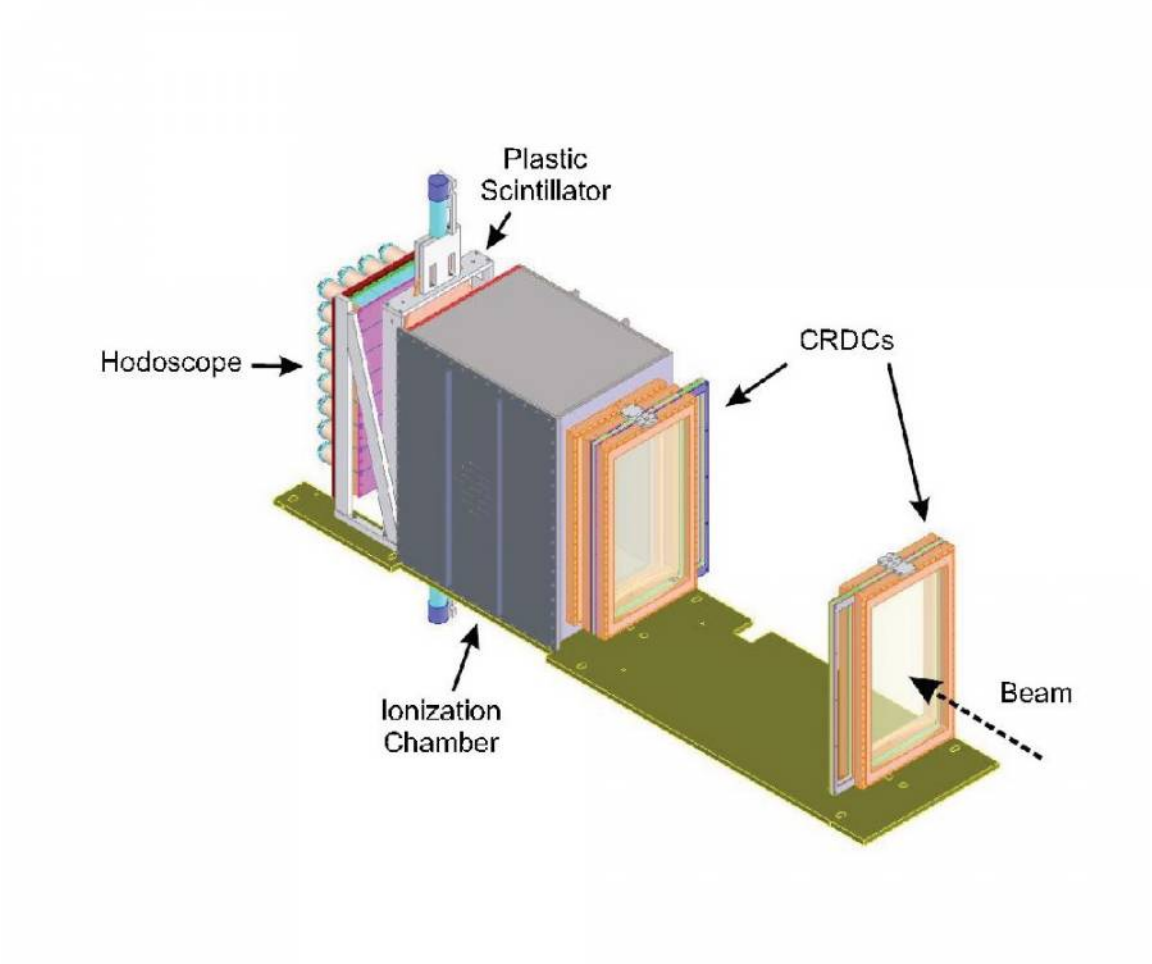


Figure 3.5: A schematic of the S800 Spectrograph Focal Plane. Image source: https://wikihost.nscl.msu.edu/S800Doc/lib/exe/detail.php?id=detectors&media=wiki:s800_fp_detectors.jpg

Cathode Readout Drift Chambers

The first detectors in the S800 focal plane through which the beam passes are the Cathode Readout Drift Chambers (CRDCs). There are two CRDCs that are 1 m apart, giving the position and angle information in both dispersive (x) and non-dispersive (y) directions with a position resolution of 0.5 mm in both directions (Fig. 3.6).

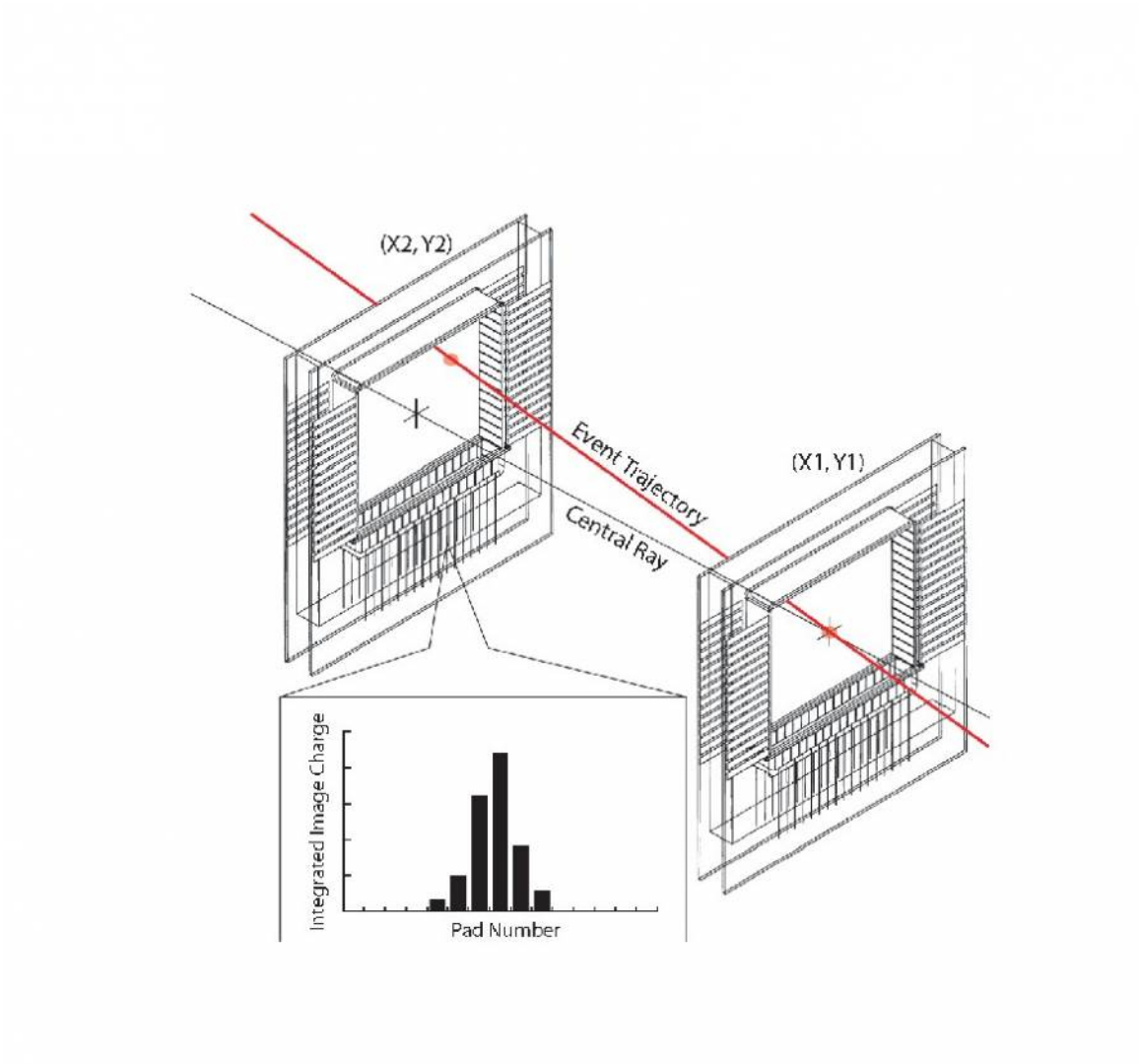


Figure 3.6: A schematic view of CRDC. Image source: https://wikihost.nscl.msu.edu/S800Doc/doku.php/id=detectors/ionization_chamber

The CRDC detectors are filled with a gas mixture of 80% CF_4 (carbon tetra-fluoride) and 20% C_4H_{10} (isobutane) at 40 Torr pressure. There is an anode wire at a positive voltage,

and the negatively biased cathode is segmented into 224 pads to collect the charge from the chamber (see Fig. 3.7). When charged particles pass through the detector, ionization is induced in the gas, producing free electrons. These free electrons drift towards the positively charged anode wire. The cathode pads are located in front of and behind the anode wire. They collect the positive charge induced by the anode. The centroid of a Gaussian fit to the charge distribution gives the dispersive (x) position. The non-dispersive (y) position is calculated using the drift time of the electrons, which is measured as the time between the E1 scintillator and the anode wire signal. A typical drift time is about 20 μs and thus the maximum rate is ≈5000 particles per second. The position measurements from the CRDCs enable the event-by-event trajectory reconstruction in the focal plane.

Inverse map

The CRDCs provide the position measurements of the particles in the dispersive (x) and non-dispersive (y) directions at two positions along the beam axis (see Fig. 3.6). The dispersive (a_{fp}) and non-dispersive (b_{fp}) angles are defined with respect to the z-axis in the xz-plane and yz-plane, respectively. The angles are given by:

$$a_{\mathrm{fp}} = \frac{\tan^{-1}(x_2 - x_1)}{d}, \tag{3.1}$$

$$b_{\mathrm{fp}} = \frac{\tan^{-1}(y_2 - y_1)}{d}, \tag{3.2}$$

where x_1 (x_2) and y_1 (y_2) are the positions provided by CRDC1 (CRDC2), and $d = 1073$ mm, is the distance between the two CRDCs.

The positions and angles of the particles in the focal plane are measured using the CRDCs, but what is needed are the positions (x_{ta}, y_{ta}), angles (a_{ta}, b_{ta}), and momenta of the particles at the target position. This enables the reconstruction of the momentum distribution. The fragment positions and angles at the focal plane and target positions are related using the inverse mapping. The inverse map uses the ion optics code COSY

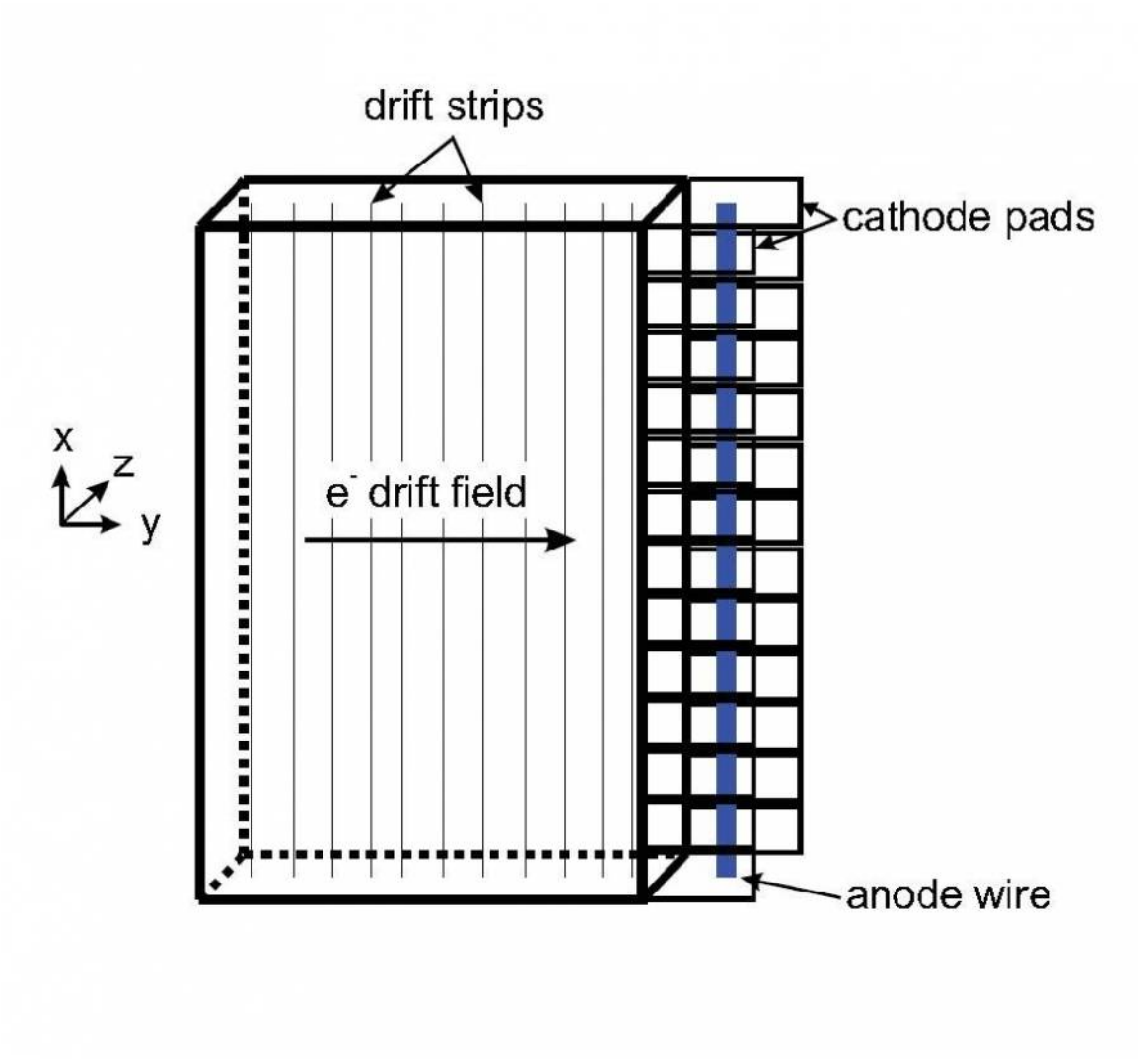


Figure 3.7: The principle of operation of a CRDC. Image source: https://wikihost.nscl.msu.edu/S800Doc/doku.php/id=detectors/ionization_chamber

INFINITY [24], to calculate the transfer matrix and thus reconstruct the target coordinates from the focal plane coordinates.

Ionization Chamber

The ionization chamber is used for particle identification (Fig. 3.8). It identifies the charge of the transmitted nuclei from their energy loss. The chamber consists of 16 stacked parallel plates with anode and cathode pairs perpendicular to the beam direction, filled with P10 gas (90% argon and 10% methane) at a pressure of 300 Torr. The positively charged beam passes through the chamber and ionizes the gas to create free electrons and positively charged gas ions. The free electrons drift towards the anode and the gas ions towards the cathode. The amount of gas ionized by a particle represents the energy loss of that particle given by the Bethe formula. The energy resolution is 1.2%.

The energy loss in the chamber is proportional to the square of charge of the particle. Therefore particles with different charges can be identified from their energy loss measurement.

Scintillators

Several scintillators measure the time-of-flight of the beam and the residual nuclei, which can be used for particle identification. The S800 includes plastic scintillators at the object and focal-plane stations. The scintillator located at the end of the fragment separator is called the x focal plane (xfp) scintillator and the one at the beginning of the S800 is the object (obj) scintillator. There is another scintillator detector at the exit window of the ionization chamber, the E1 scintillator. The difference between the E1 and obj/xfp timing signals provides the time-of-flight of the beam-like particles. The timing resolution for a point-like beam spot in the focal plane is 170 ps. The charged particles are dispersed by the S800 magnetic dipoles according to their magnetic rigidity. Particles with a large mass-to-charge ratio are bent less in the dipole leading to a longer flight path. Thus, the measured time-of-flight can be used to distinguish between different isotopes.



Figure 3.8: Ionization Chamber. Image source: https://wikihost.nscl.msu.edu/S800Doc/doku.phpid=detectors_ionization_chamber

3.4 GRETINA

The Gamma-Ray Energy Tracking In-beam Nuclear Array (GRETINA) is a γ-ray detection system consisting of 48 highly segmented High-Purity Germanium (HPGe) crystals that can track the interaction of γ rays within the crystal volume [25, 26]. Each crystal has 36 electrically isolated outer contacts and a central core contact for a total of 37 electrical readouts from each crystal. Four crystals are combined in a single cryostat to form a quad-crystal module. Twelve such quad-crystal modules were used in this experiment. The central core contact gives the best energy resolution of the gamma ray interaction, and the high segmentation of each crystal allows for the reconstruction of gamma ray interactions from multiple individual Compton scatter and photoelectric absorption events to achieve a position resolution of $\approx$2 mm. The energies of γ rays measured in the lab frame with the GRETINA are Doppler corrected for shifts as the reaction residues are moving at relativistic speeds.

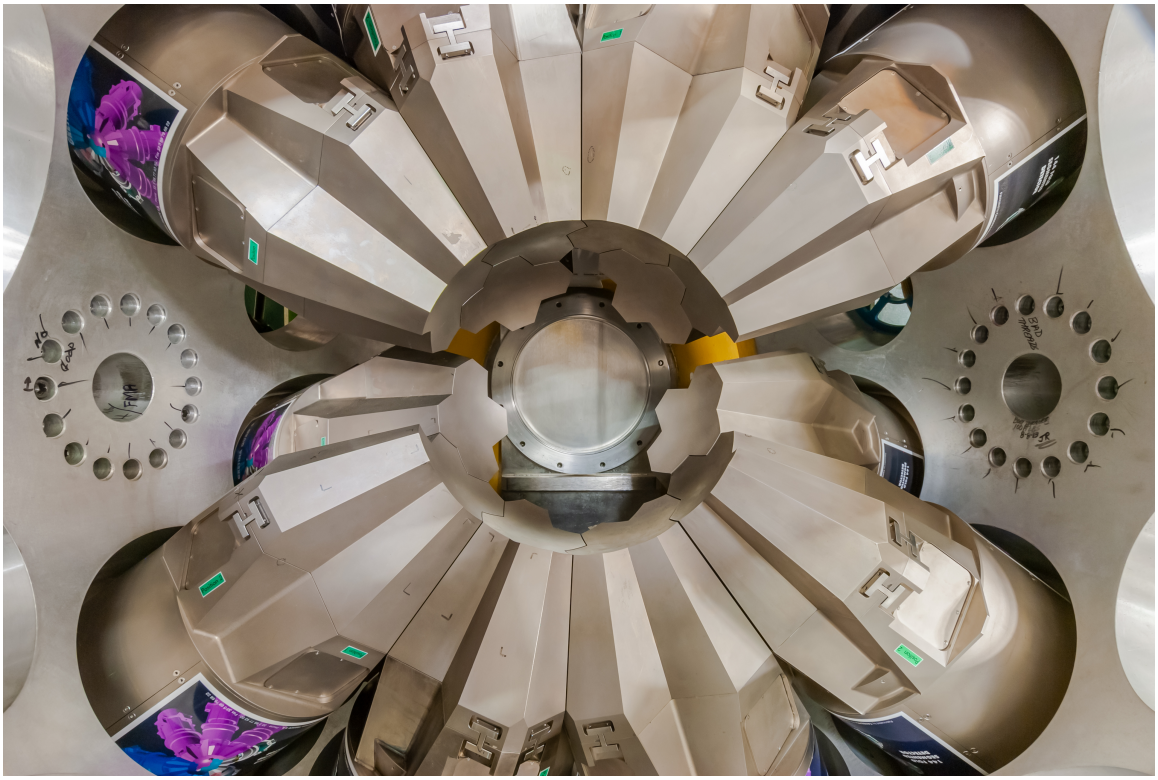


Figure 3.9: A "beam-view" shot (from the upstream looking towards the S800 Spectrograph). Image source: https://people.nscl.msu.edu/noji/gret12det

Chapter 4

Analysis

The momentum distributions of the residue resulting from the single neutron knockout reaction on ^{106}Sn beam reflect the orbital angular momentum (l-value) of the removed neutron. To measure the parallel momentum distributions of the ground and first excited states in ^{105}Sn, we reconstruct the parallel momentum at the target position from the position and angle of ^{105}Sn in the focal plane of S800, gating on γ-rays in GRETINA to select the populated states. This can be achieved only after performing calibrations and corrections to the measured values so that we can separate the ^{106}Sn in the incoming beam from other contaminants that are present in the beam and construct a residue Particle Identification Diagram (PID) of the reaction products, where we can separate ^{105}Sn from other products. The GRETINA γ rays have to be Doppler corrected so that we can clearly select the transitions of interest.

This chapter describes the calibrations and treatment of recorded data prior to deducting the physical observables. The first five sections describe the calibrations of S800 detectors, followed by the particle identification. In Sec. 4.5, γ-ray analysis from GRETINA will be discussed, followed by the GEANT4-UCGretina simulations (Sec. 4.6). The momentum distribution and cross section calculations are presented towards the end of this chapter (Sections 4.7 and 4.8).

4.1 Ionization Chamber calibration: Gain Match

The energy loss measurement for a portion of the gas in the ionization chamber is given by each of the 16 channels in it. The total energy lost in the IC is the sum of the energy lost in each channel:

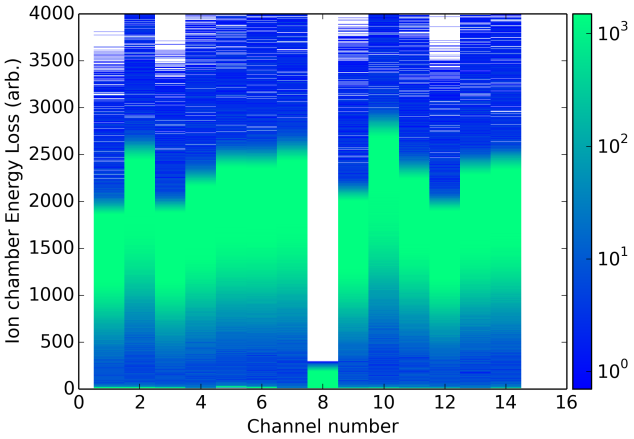
$$E_{\text{sum}} = \sum_{i=1}^{16} E_i, \tag{4.1}$$

where E_{sum} is the total energy lost in the ionization chamber and E_i is the energy lost in the i^{th} channel.

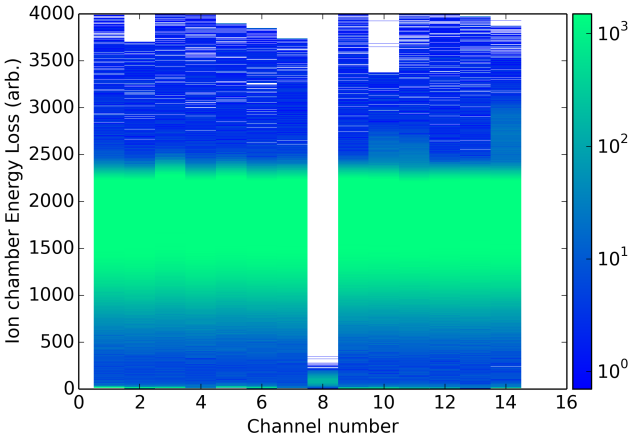
The raw energy loss of each channel differs, and since the total energy is the sum of energy loss in each channel, the energy spectrum for each channel should be gain matched to one of the channels. This is done by calculating the centroid of the energy loss for the isotopes in all 16 channels of the ionization chamber. These centroids provide points for determining a linear function to gain match each channel to the selected channel (see Fig. 4.1).

4.2 Cathode Readout Drift Chamber calibration: Mask Calibration

The non-dispersive position of the particle in the CRDC is determined by the drift time of the electrons. This depends on the properties of gas in each CRDC and it can change over time. Therefore a mask calibration is performed using masks with holes at known positions (Fig. 4.2a). They are inserted directly in front of each CRDC. These mask runs are used to fit the measured y positions to the known y positions in the mask using a linear function. The calibrated spectrum is given in Figure 4.2b.

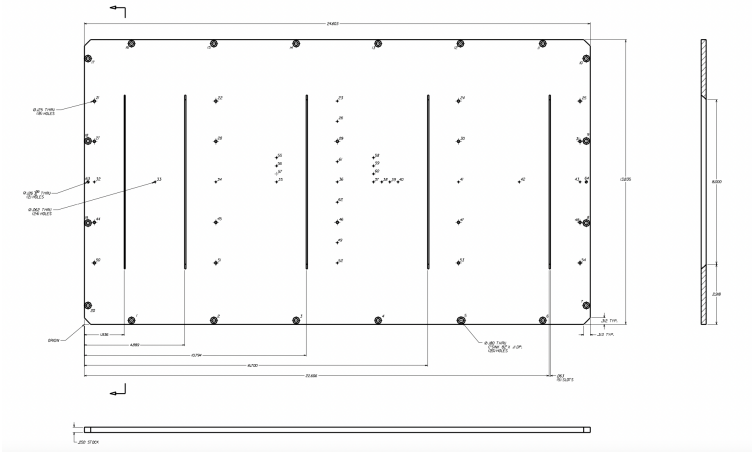


(a)

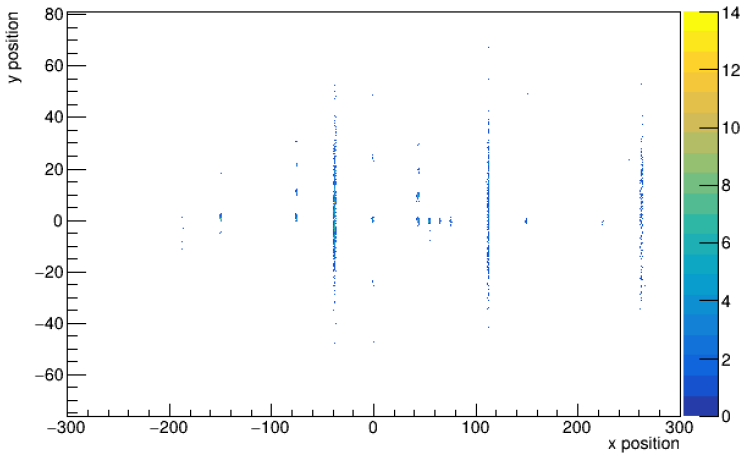


(b)

Figure 4.1: The energy loss signal in each ion chamber must be matched. Plots of the uncalibrated (a) and the calibrated (b) energy loss measurements are shown for each channel of the ionization chamber. Channel 7 was not working.



(a)



(b)

Figure 4.2: (a) The mask pattern used for the calibration from https://wikihost.nscl.msu.edu/S800Doc/lib/exe/fetch.php/media=wiki:mask.pdf. (b) The X versus Y positions recorded by the first CRDC are plotted for a mask calibration run. The mask pattern is clearly visible.

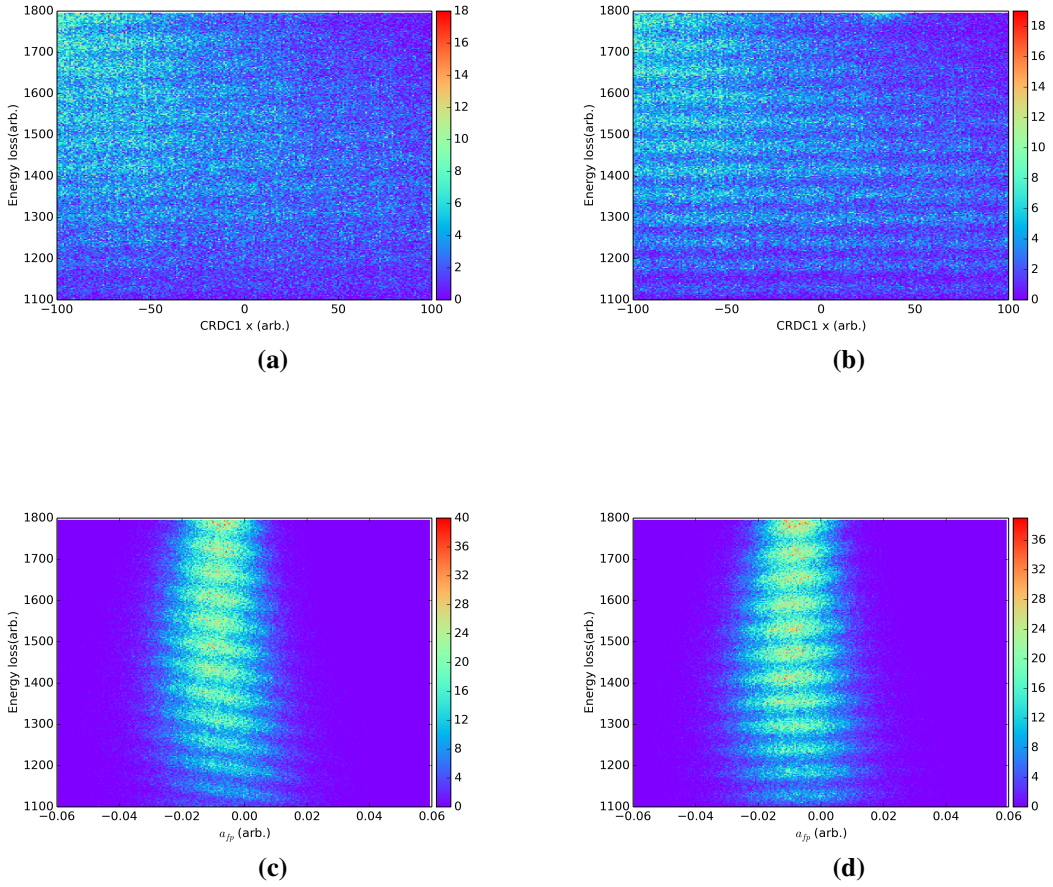


Figure 4.3: Ionization chamber energy loss as a function of dispersive position (x) and angle (a_{fp}) at CRDC1. Panels (a,b) show uncorrected and corrected spectra versus dispersive position, while (c,d) show the corresponding spectra versus dispersive angle.

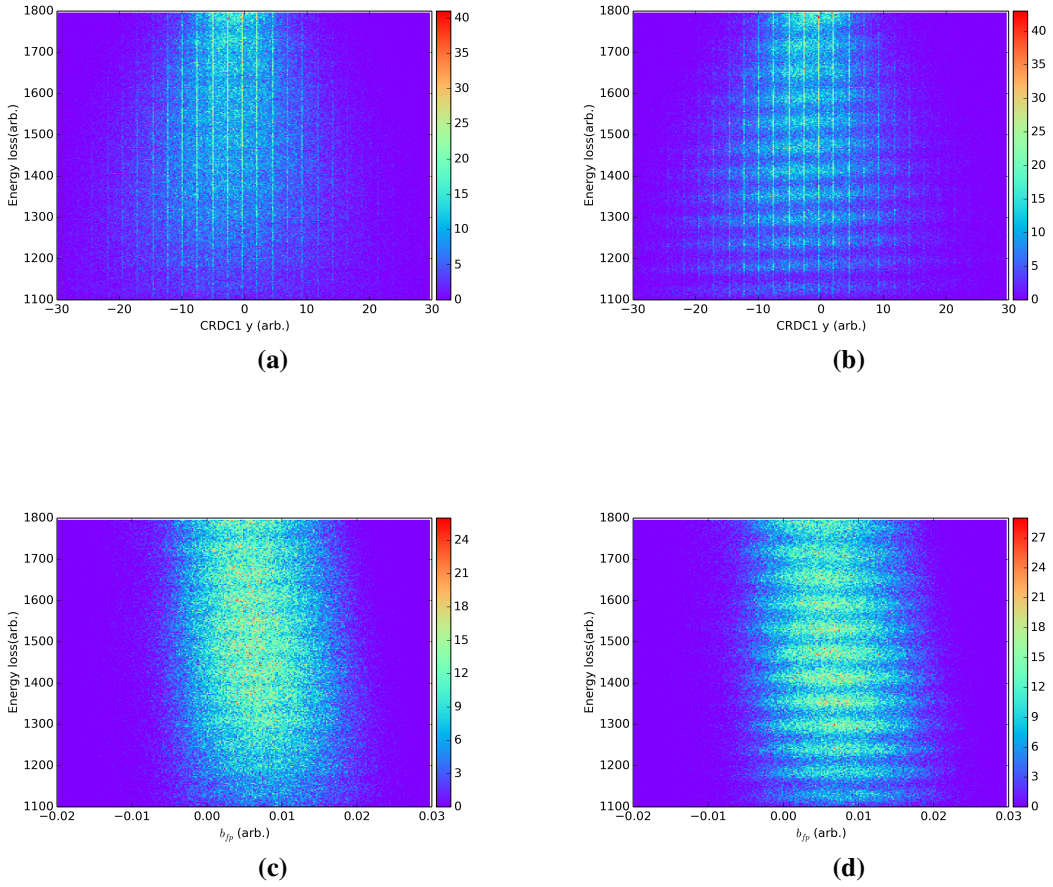


Figure 4.4: Energy loss as a function of non-dispersive position (y) and angle (b_{fp}) at CRDC1. Panels (a,b) show uncorrected and corrected spectra versus position y, while (c,d) show the corresponding spectra versus angle b_{fp}.

4.3 Ionization chamber calibration: Position Correction

The energy loss also varies as a function of the position and angle of the particle in the ionization chamber. So a correction to account for this is applied. The energy loss for the isotopes versus the dispersive and non-dispersive positions and angles measured in the CRDC is plotted, giving variation with respect to position and angles. The relation showing the energy loss and position is given by the following formula:

$$E_{\mathrm{cor}} = E_{\mathrm{ic}}(1 + y_{\mathrm{tilt}}\, y \,+\, b_{\mathrm{fp}}\, b_{\mathrm{tilt}})\ \exp\,(x_{\mathrm{tilt}}(x_0 - x)\ \exp\,(a_{\mathrm{tilt}}(a_0 - a_{\mathrm{fp}}), \tag{4.2}$$

where E_{cor} is the corrected energy value, E_{ic} is the energy from the IC, x_{tilt} (y_{tilt}) are the x (y) correction parameters, x (y) are the dispersive (non-dispersive) positions, a_{tilt} and b_{tilt} are the correction parameters for dispersive and non-dispersive angles (a_{fp} and b_{fp}), x_0 and a_0 are the position and angle measured in CRDC1. Figures 4.3 and 4.4 show the energy spectra before and after corrections to the dispersive and non-dispersive positions and angles, applied according to Equation 4.2.

4.4 Time of Flight correction

As mentioned in section 3.3.1, the plastic scintillators at the end of fragment seperator (XFP), the beginning of the S800 (OBJ), and the exit window of the ionization chamber (E1) provide the time-of-flight measurements of particles. The incoming particle identification was performed using the two dimensional plot between the two time-of-flight measurements, XFP-E1 and OBJ-E1, whereas the outgoing particles were identified using the combination of energy loss measured in the ionization chamber and the OBJ-E1 time-of-flight.

Particles of the same isotope pass through the S800 somewhat differently due to variations in the energy loss in the target and scattering angle. This results in time-of-flight spread due to the variation in flight path. To minimize this effect, corrections are

applied to the time-of-flight using both dispersive and non-dispersive angles and positions by assuming linear dependences of these parameters, according to the formula:

$$\Delta t_{\text{corr}} = \Delta t + m\, a_{\text{fp}} + n\, b_{\text{fp}} + p\, x_1 + q\, y_1, \tag{4.3}$$

where a_{fp} and b_{fp} are the angles in the dispersive and non-dispersive directions, x is the x-position of the particle in the most upstream CRDC and y is the y-position in the CRDC. Parameters m, n, p, and q are varied to maximize separation of reaction products. The correction parameters are correlated; therefore, one parameter is optimized and fixed before adjusting the other. This procedure is repeated iteratively until the best time-of-flight resolution is achieved. The purpose of the correction is to determine the optimal values of these fitting parameters, and the calculations are performed after applying a gate on the tin region in the incoming PID spectrum. The results after applying the corrections can be seen in Figures 4.5 , 4.6, 4.7 and 4.8.

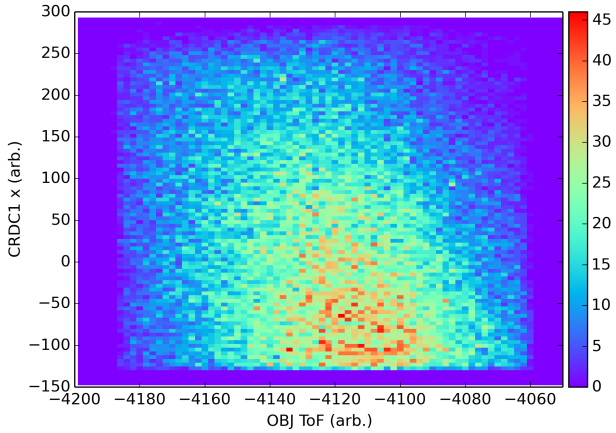
4.5 GRETINA Analysis

4.5.1 Doppler Correction

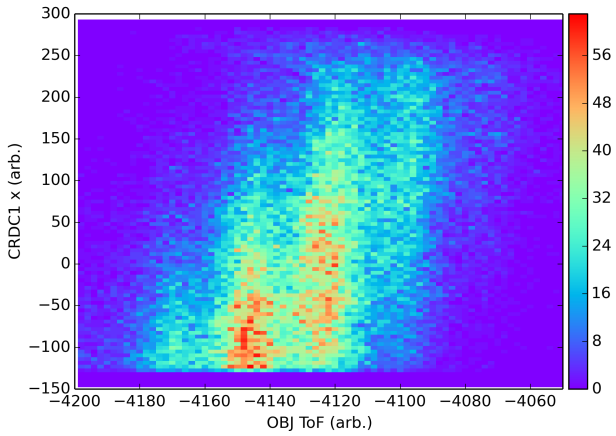
The gamma rays that come from a nucleus in motion experience a Doppler shift. This causes the energy observed in the lab frame to be different from the energy emitted in the center of mass frame. Thus, the detected energy needs to be corrected to obtain the true energy of the gamma ray. The Doppler shift depends on the angle between the nuclear velocity direction and the γ-ray emission, as well as the velocity magnitude β. The relation between energy in the laboratory frame E_{lab} and the gamma energy in the center of mass frame E_{cm} is given by

$$E_{\text{cm}} = E_{\text{lab}} \frac{1 - \beta \cos\theta}{\sqrt{1-\beta^2}} \tag{4.4}$$

where β is the fraction of the speed of light $\frac{v}{c}$ and θ is the separation angle between the γ-ray and the particle (Fig.4.9). $\cos\theta$ can be obtained from the (θ, ϕ) coordinates of the

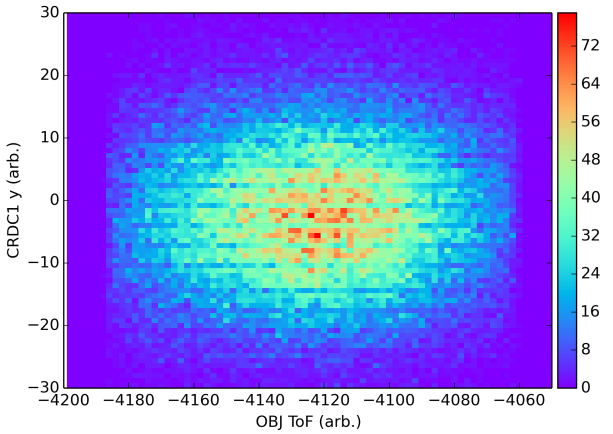


(a)

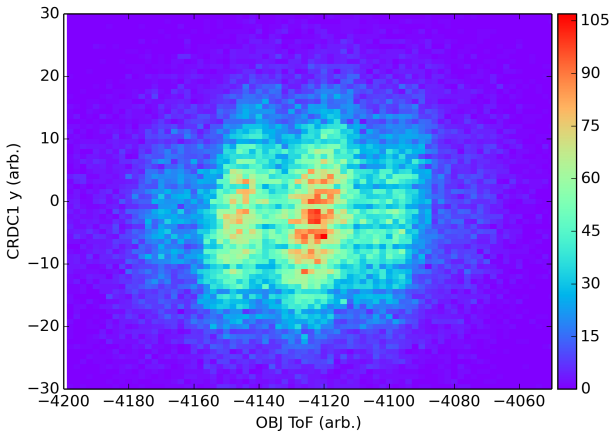


(b)

Figure 4.5: The TOF is plotted with respect to the x (dispersive) position of the particles. The uncorrected spectrum (a) indicates that the TOF varies greatly depending on the position. This spread causes the TOF of the isotopes to overlap. The corrected (b) shows the result after adjusting the TOF for the position of the particle.

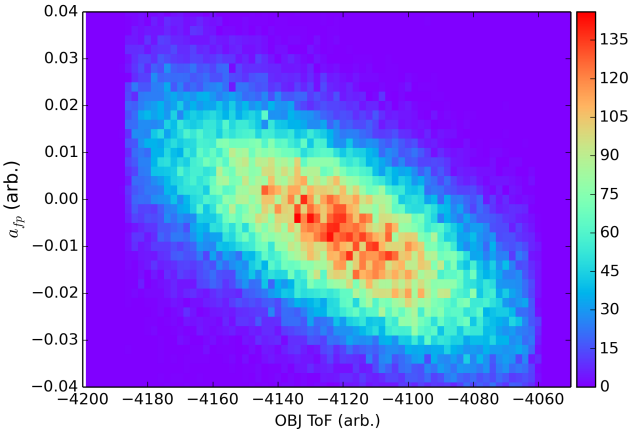


(a)

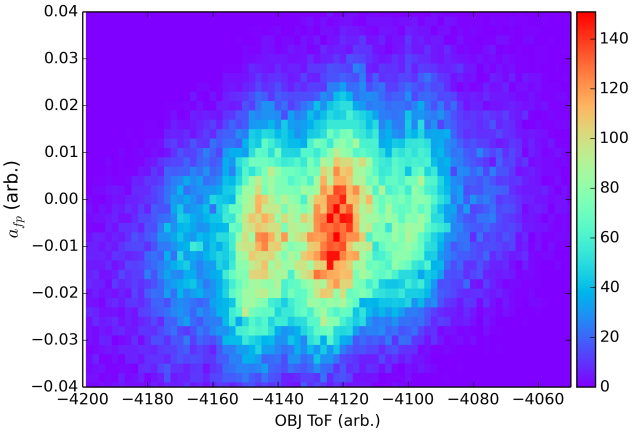


(b)

Figure 4.6: The TOF is plotted with respect to the y (non-dispersive) position of the particles. The uncorrected spectrum (a) and the corrected spectrum (b)

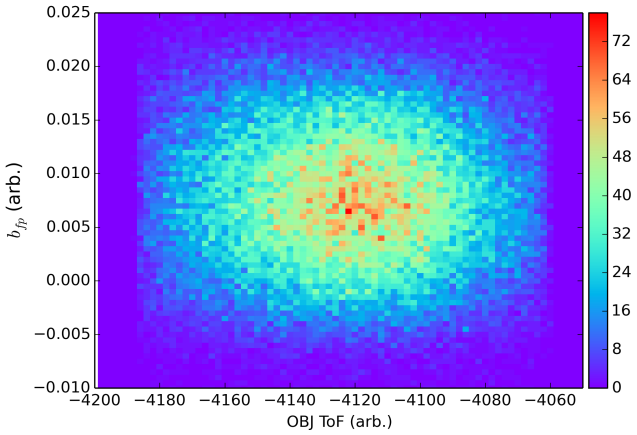


(a)

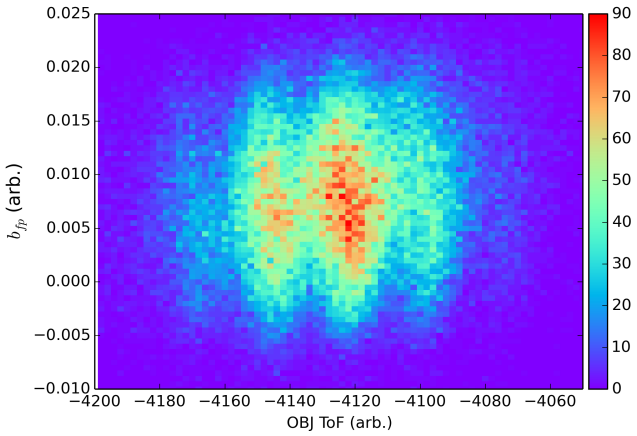


(b)

Figure 4.7: The TOF is plotted with respect to their trajectory angle (a_{fp}) in the dispersive position of the particles. In the uncorrected (a) spectrum, it is impossible to distinguish between the isotopes. The corrected (b) spectrum shows them much more clearly.



(a)



(b)

Figure 4.8: The TOF is plotted with respect to their trajectory angle (b_{fp}) in the non-dispersive position of the particles. The uncorrected (a) and corrected spectrum (b).

particle and γ-ray using the equation given below:

$$\cos\theta = \sin\theta_{\text{part}} \sin\theta_{\gamma} \cos(\phi_{\text{part}} - \phi_{\gamma}) + \cos\theta_{\text{part}} \cos\theta_{\gamma}. \tag{4.5}$$

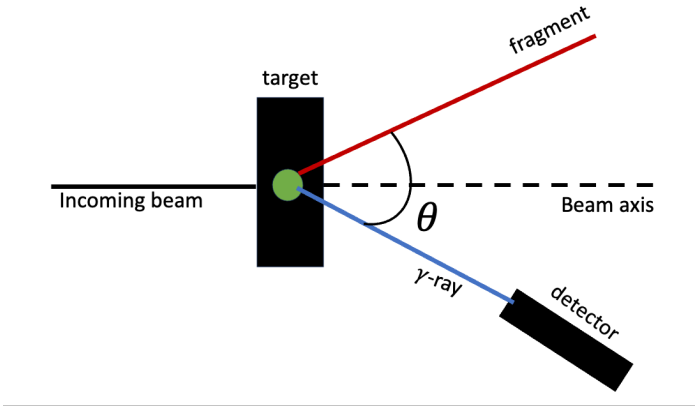


Figure 4.9: Schematic diagram illustrating the geometry used for Doppler correction of emitted γ rays. The emitted γ ray is detected at an angle θ with respect to the fragment velocity vector

Converting Doppler-shifted γ-ray energies to the center of mass frame energies requires accurate knowledge of two parameters, β and θ. The θ_{part} and ϕ_{part} components of the angle are determined from the dispersive and non-dispersive angles at the target, a_{ta} and b_{ta}, respectively, obtained from the inverse mapping (Sec.3.3.1) from the position of the particle at S800 focal plane. θ_{γ} and ϕ_{γ} components are determined from the interaction points measured by GRETINA, and an assumed emission position, usually at or near the nominal target position. Several empirical corrections to the assumed decay position and recoil directions obtained from the inverse mapping are applied to optimize the Doppler-corrected energy resolution. Figure 4.10 depicts the level scheme for ^{105}Sn, including transition energies and gamma ray cascade structure. Figure 4.12b shows a Doppler-corrected spectrum with peaks representing the γ-ray transitions shown in the level scheme. Figure 4.12a shows significant background contributions from neutron-induced processes,

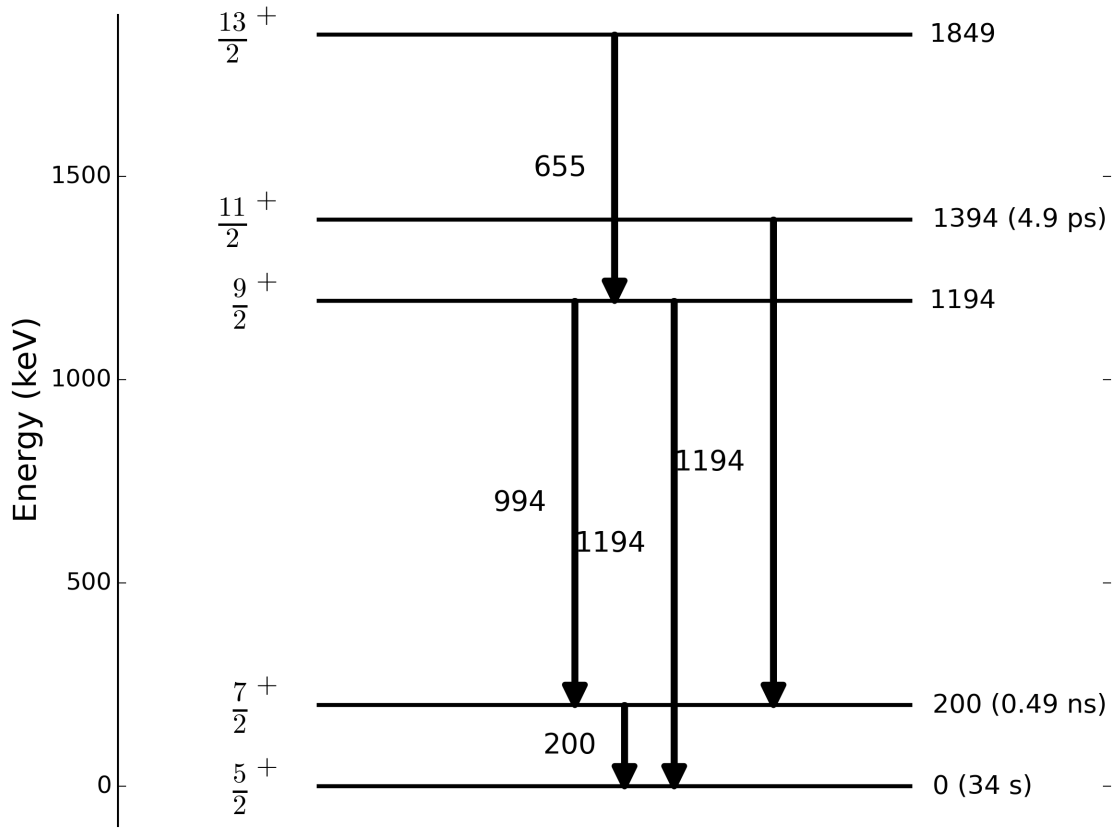


Figure 4.10: The figure shows the level scheme of ^{105}Sn as taken from the ENSDF [10]. The energies of the levels, together with their half-lives, are shown on the right, while spin-parity for levels is shown on the left. The energy of transitions is represented by transition arrows. The energies are in keV.

which come from the stationary sources from the detector or beam pipe, as discussed in Section 4.6.1. Doppler correction, which assumes emission from moving reaction products, smears out the background γ-rays in the corrected spectrum.

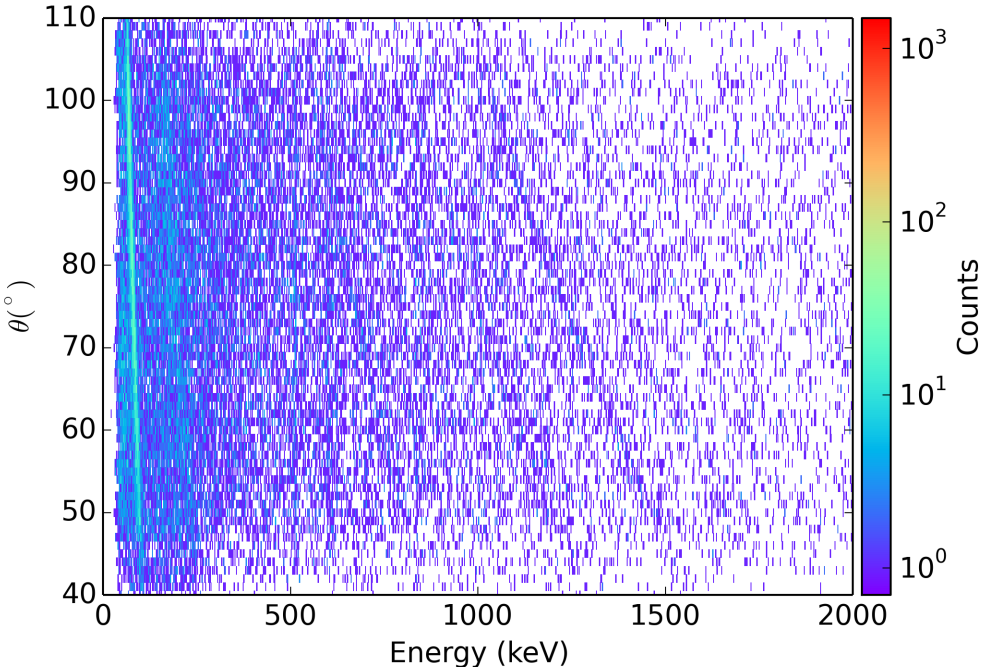
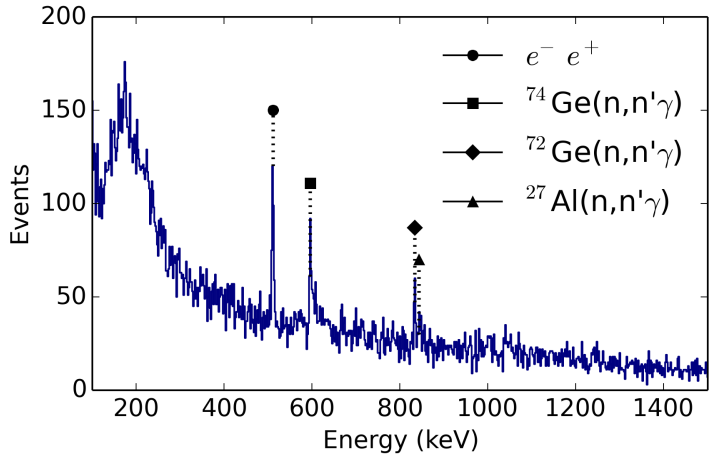
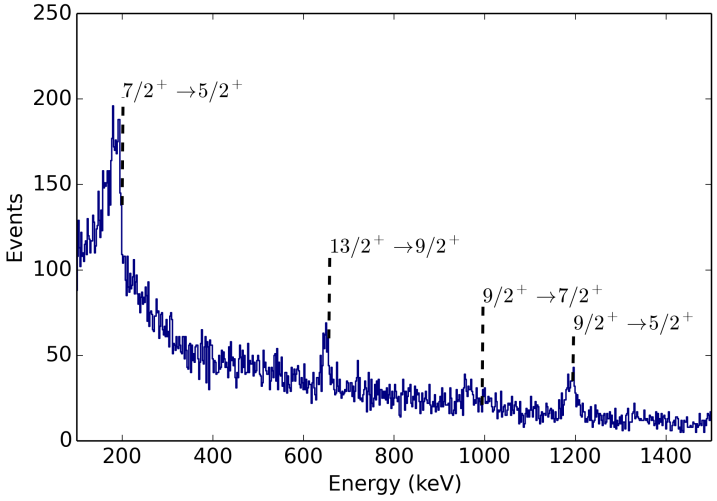


Figure 4.11: The x-axis represents detected gamma ray energy (keV), whereas the y-axis represents the measured gamma ray emission angle (in degrees). The vertical structures indicate gamma rays from neutron-induced events in stationary backgrounds, whereas the slanted lines represent transition gamma rays.



(a)



(b)

Figure 4.12: The gamma ray spectrum for ^{105}Sn before (a) and after (b) applying Doppler corrections. The top spectrum presents laboratory frame gamma spectra with peaks corresponding to numerous background neutron-induced reactions, whereas the bottom spectrum shows how these peaks disappear after Doppler shift correction and the knockout reaction peaks become visible.

4.6 GEANT4-UCGretina Simulation

The Ursinus College Gretina simulation code (UCGretina) [27] is a GEANT4 simulation [28] code that simulates the response of GRETINA to gamma rays from decay sources and nuclear reactions. It uses a collection of models best suited to low-energy physics applications and for experiments with in-beam measurements. Beam nuclei are tracked through the target and undergo gamma decay in flight. The simulation includes energy loss of the beam through the target, Compton scattering in the detector volume and other non-detector materials, as well as the position resolution of interactions in GRETINA. We specify the detector geometry and experimental parameters, such as target thickness and incoming beam energy, and obtain a simulated spectrum which can be compared with the experimental Doppler-corrected spectrum.

To specify the energy of the secondary incoming beam in the simulation, S800 analysis line rigidity settings from before the target were used. For the outgoing beam energy, S800 rigidity after the target were used. LISE++ [29] was used to convert between rigidity and energy. These parameters are necessary for accurate simulations to match the experimental data. The incoming secondary beam energy of 83.35 MeV/u for ^{106}Sn beam was calculated from the S800 rigidity setting $B\rho = 2.85$ Tm for the reaction setting runs. The outgoing residue energy for ^{105}Sn after the target was calculated as 74.50 MeV/u from the S800 rigidity setting $B\rho = 2.66$ Tm. These information is summarized in Table 4.1. The response functions for each state in the residual nucleus are generated with these energy values and are shown in Figure 4.13.

Table 4.1: Summary table of beam settings before target and reaction settings after target.

Location	Species	Bρ (Tm)	E (MeV/nucleon)
Analysis line(before target)	^{106}Sn	2.85	83.35
S800(after target)	^{105}Sn	2.66	74.50

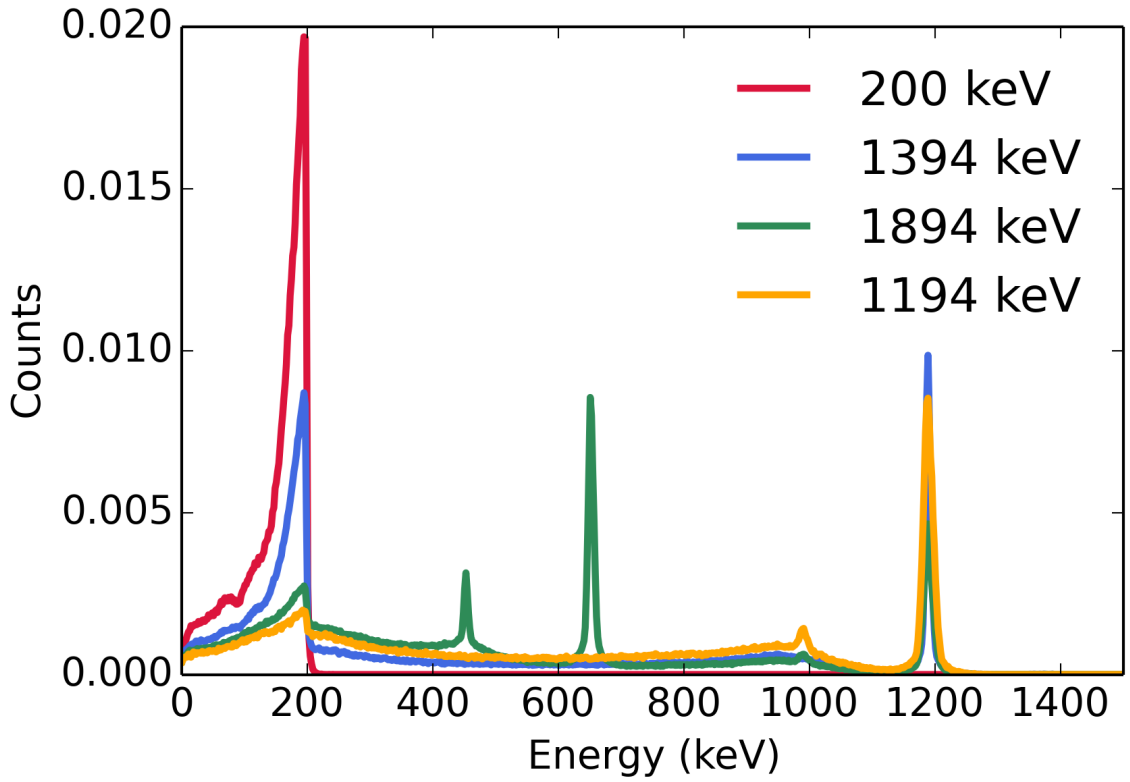


Figure 4.13: Simulated response functions for excited states 200 kev, 1194 keV, 1394 keV and 1849 keV.

4.6.1 FitGretina

The UCGretina simulations give a response function for each possible state in the residual nucleus that could be populated by the knockout reaction (Fig. 4.13). The response function histograms are scaled appropriately so that their sum closely matches the experimental spectrum. FitGretina [30] is a program that fits the experimental spectrum by finding these optimal scaling amplitudes. The scaling factors reflect the relative population amplitudes of each excited state populated in the reaction.

In addition to the response functions from the residual nucleus, there are two kinds of background that must be accounted for: non-correlated and correlated backgrounds. Non-correlated background consists of gamma rays that are not induced by the beam. Examples of such backgrounds include the natural radioactive contamination from ^{40}K or the gamma rays from the natural decay series of radon. These are accounted for by providing an experimental non-prompt spectrum in which the gamma ray and particle are not coincident.

The second type of background is the correlated background, induced by the beam. In knockout reactions, a large number of neutrons are produced by the beam and inelastically scatter or otherwise react with material nearby. In addition, there may be a beam halo present, which is incident on parts of the beam pipe, target holder, etc. All these reactions can produce gamma rays, which are correlated with the beam and, therefore cannot be easily isolated. They are accounted for in the simulation in two ways. Firstly, by simulating a loosely forward-focused distribution of neutrons at various energies; in this work, the energies range from 1 to 60 MeV. The gamma rays produced from this background are often relatively stationary in the lab frame and hence are generally not strongly Doppler shifted. Thus, in the Doppler-shifted spectrum, they appear as broad features instead of distinct, sharp transitions and are not easily constrained. For this reason, FitGretina fits both Doppler-corrected and non-Doppler-corrected spectra simultaneously, as the non-Doppler-corrected spectrum exhibits sharp lines corresponding to the neutron background, which serves to constrain the magnitude of this background. Secondly, FitGretina also includes an exponential function as an empirical background estimate.

In this work, two Doppler-corrected gamma spectra are created, based on the total gamma multiplicity of the event, γ_{mul}. The spectrum with $\gamma_{\text{mul}} = 1$ exhibits a noticeably reduced background in the low-energy region compared to the ungated spectra. The gamma multiplicity gate has less sensitivity to the background shapes for extracting lifetimes (see Sec. 4.6.2), and gives some sensitivity to placing unknown transitions in the level scheme. In contrast, the $\gamma_{\text{mul}} > 1$ spectrum preferentially shows transitions in cascades, where many γ rays are emitted simultaneously. Both $\gamma_{\text{mul}} = 1$ and $\gamma_{\text{mul}} > 1$ spectra are fitted separately.

4.6.2 Lifetime measurements

When a beam nucleus reacts with a target nucleus, the reaction products can be formed in excited states, which then decay by emitting a gamma ray, transitioning to a lower energy state. The formula for the time-dependence of these decays is shown below:

$$N(t) = N_0 e^{-t/\tau}, \tag{4.6}$$

where N is the number of particles remaining as a function of time, N_0 is the initial number of particles, and τ is the lifetime of the excited state. The lifetime and half-life are related by the formula:

$$T_{1/2} = \tau \ln 2 \tag{4.7}$$

The observed shape of a γ-ray peak is related to the lifetime of the emitting nuclear state. For short-lived states, the γ-ray is emitted either from inside the target nucleus or almost immediately as the residue exits the target, resulting in a narrow peak after Doppler correction due to the accurate reconstruction of the emitted γ-ray angle. In contrast, for long-lived states, the nucleus travels a finite distance before decay. Consequently, γ-rays are emitted over a range of positions downstream of the target, producing a broadened or asymmetric peak in the reconstructed energy spectrum (Fig 4.14). The Doppler-broadened lineshape thus encodes the position distribution of the emitting nucleus at the time of emission. If the velocity of the outgoing nulceus is known, this can be used to extract

the lifetime of the excited state. For this work, beam has β-value of ≈ 0.4, and the beam traverse ≈ 12 cm/ns through the target thickness, and therefore for states with half-lives of the order of 100 ps and greater, the majority of decays take place downstream of the target.

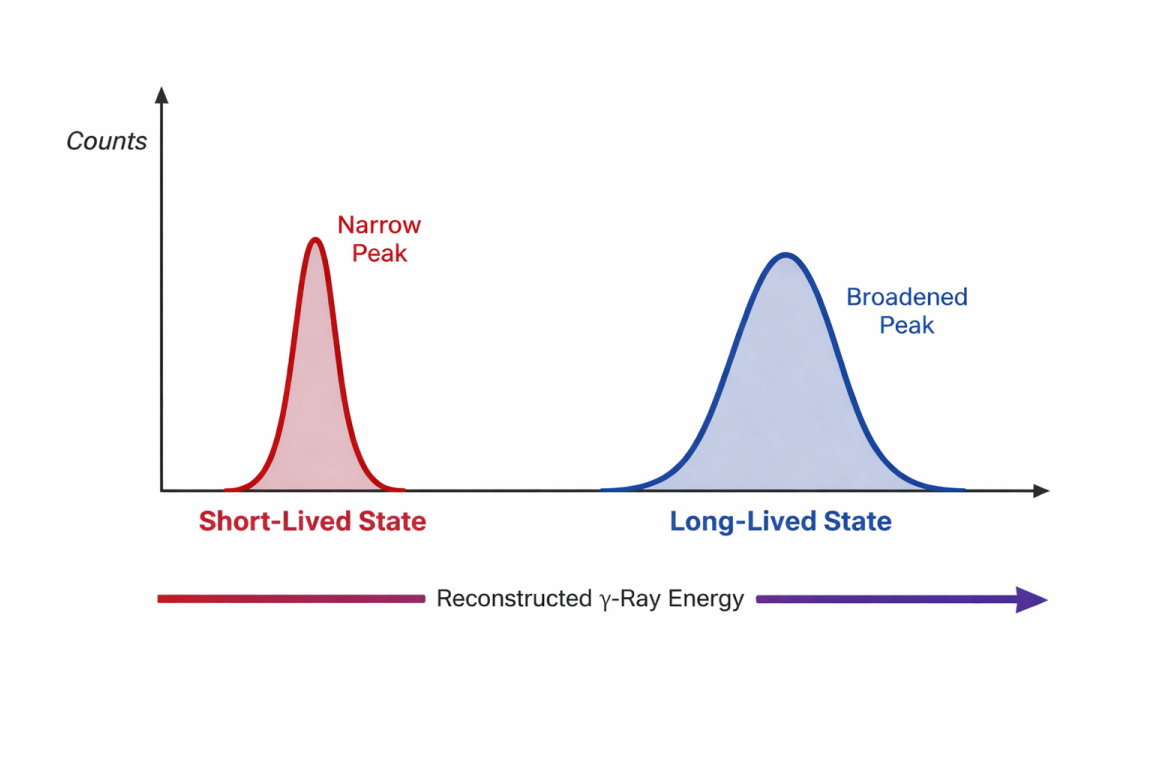


Figure 4.14: A short-lived state gives narrow peak and long-lived state results in broadened peak

The lifetime of the excited nuclear state was extracted using a minimum chi-square fitting procedure applied to Doppler-corrected γ-ray energy spectra measured with the GRETINA array. The experimental spectra were compared to the simulated response functions generated using the UCGretina simulation framework.

UCGretina simulations were performed for a range of assumed lifetimes for the first excited state, incorporating the full experimental detector geometry, reaction kinematics, beam energy, and target details. The simulations account for Doppler broadening effects arising from the finite lifetime of the excited state, including the slowing down of the recoiling nucleus in the target prior to γ-decay. The spectra are fitted using the FitGretina code, which provides a chi-square value for the fitted 200 keV peak that corresponds to the

transition from the first excited state to the ground state. Chi-square values were calculated to quantify the agreement between the experimental and simulated spectra:

$$\chi^2(T_{1/2}) = \sum_i \frac{\left[N_i^{\text{exp}} - N_i^{\text{sim}}(T_{1/2})\right]^2}{\sigma_i^2}, \tag{4.8}$$

where N_i^{exp} and N_i^{sim} are the experimental and simulated counts in the energy bin i respectively and σ_i denotes the statistical uncertainty of the experimental data.

The best-fit half-life corresponds to the value of $T_{1/2}$ for which the chi-square function reaches its minimum, χ^2_{min}. The uncertainty in the extracted half-life was determined using the criterion,

$$\chi^2(T_{1/2}) = \chi^2_{\text{min}} + 1, \tag{4.9}$$

which corresponds to a one-standard-deviation confidence interval. The lower and upper bounds of the half-life uncertainty were obtained from the values of $T_{1/2}$ at which this condition is satisfied.

4.7 Momentum Distribution Calculations

The high acceptance and high resolution for S800 are achieved from the technique of particle trajectory reconstruction, where the ion optical code COSY Infinity [24] generates an inverse map for each recoil [31] that relates the dispersive and non-dispersive positions (x_{fp}, y_{fp}) and corresponding angles (a_{fp}, b_{fp}) of a particle at the focal plane to the new variables, a_{ta}, b_{ta}, y_{ta} and d_{ta}, which are the dispersive and non-dispersive angles at the target, the non-dispersive position of the particle at the target, and the relative energy ($d_{\text{ta}} = \frac{E-E_0}{E_0}$), E is the energy of the outgoing particle. The relation between these variables

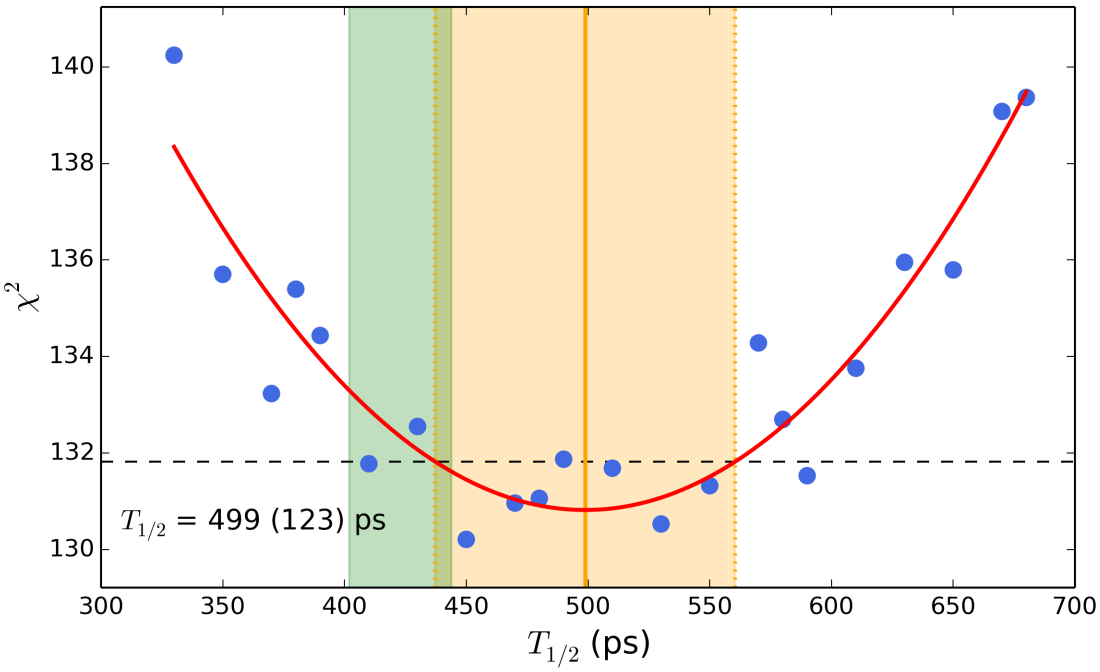


Figure 4.15: χ^2 fitting for the simulated half-life and uncertainty determined from the one-standard-deviation confidence interval. The blue points represent the χ^2 values from the simulations for different half-life values shown on the x-axis. The red curve is the quadratic fit to the χ^2 distribution. The horizontal dashed line indicates the $\chi^2_{\text{min}} + 1$ level, which defines the uncertainty limits on the half-life. The green shaded region represents the previously reported half-life from the work [11], and the orange shaded region is the half-life range obtained in the present work.

can be written as:

$$\begin{pmatrix} a_{\text{ta}} \\ y_{\text{ta}} \\ b_{\text{ta}} \\ d_{\text{ta}} \end{pmatrix} = S^{-1} \begin{pmatrix} x_{\text{fp}} \\ a_{\text{fp}} \\ y_{\text{fp}} \\ b_{\text{fp}} \end{pmatrix}, \tag{4.10}$$

where S^{-1} denotes the inverse map.

The energy of the particle passing through the central trajectory of the S800 is calculated using the formula:

$$E_0 = M(\gamma_0 - 1). \tag{4.11}$$

The product of velocity and the relativistic parameter of the reaction residue can be calculated using the magnetic rigidity, $B\rho$ in Tm of the S800 spectrometer as follows:

$$\gamma\beta = \frac{P}{M} = \frac{B\rho Ze}{M} \approx \frac{Z}{A}.\frac{B\rho}{3.10715}, \tag{4.12}$$

where $M \approx A \times 931.502$ is the mass in MeV. The relativistic factor of the central trajectory of the S800 spectrometer is then deduced as:

$$\gamma_0 = \sqrt{1 + (\gamma_0\beta_0)^2} = \sqrt{1 + \left(\frac{B\rho_0 Ze}{M}\right)^2}. \tag{4.13}$$

Therefore, the energy of the particle can be obtained as:

$$E_0 = M\left(1 + \sqrt{\left(\frac{B\rho_0}{3.107}\frac{Z}{A}\right)^2} - 1\right). \tag{4.14}$$

The linear momentum, p, is calculated using the equation:

$$p = E\sqrt{1 + 2\frac{M}{E}}, \tag{4.15}$$

The direction of the momentum vector is deduced by,

$$\hat{P} = (\sin\theta\cos\phi,\ \sin\theta\sin\phi,\ \cos\theta) \tag{4.16}$$

and the scattering angle is calculated using the equation:

$$\theta = \sin^{-1}\left(\sqrt{\sin^2 a_{\mathrm{ta}} + \sin^2 b_{\mathrm{ta}}}\right), \tag{4.17}$$

and

$$\tan\ \phi = \frac{\sin\ b_{\mathrm{ta}}}{\sin\ a_{\mathrm{ta}}}. \tag{4.18}$$

Parallel momentum is calculated using the formula:

$$p_{||} = p\cos\theta. \tag{4.19}$$

After calculating the parallel momentum, a momentum histogram was generated with the formula $\Delta p_{||}$ = $p_{||}$ - $p^{'}_{||}$, where $p^{'}_{||}$ is the parallel momentum of the particle at $d_{\mathrm{ta}} = 0$.

4.7.1 Extracting momentum distributions for excited states

To extract momentum distributions corresponding to the direct population of each excited state, momentum-gated energy spectra are created. Each of these histograms is fitted independently with FitGretina and the common response functions for the possible excited states from the UCGretina simulations. The fitted amplitudes correspond to the direct population of each excited state as a function of $p_{||}$, accounting for efficiency and feeding from higher levels. The distribution of fitted amplitudes (for each excited state) then corresponds to the exclusive momentum distributions. In order to make spin and parity assignments, the extracted momentum distributions are compared to the momentum distribution calculated from the eikonal model [14](see Sec. 2.3).

In the eikonal model, the momenta($p_{||}$) are the residue momentum in rest frame of the projectile. Hence, the momenta and the distribution of $\frac{d\sigma}{dp_{inc}}$ in the frame of the incoming

projectile are boosted into the lab frame using the formula below:

$$\Delta p_{\text{lab}} = \gamma\left(p_{\text{inc}} + \beta\sqrt{m_0^2 + p_{\text{inc}}^2}\right) - p_0, \tag{4.20}$$

with momenta in units of MeV/c and mass in MeV/c^2

$$\beta = v/c \tag{4.21}$$

$$\gamma = \frac{1}{\sqrt{1-\beta^2}} \tag{4.22}$$

The distribution is converted using the formula below:

$$\frac{d\sigma}{dp_{\text{inc}}} = \frac{d\sigma}{dp_{\text{lab}}} \cdot \frac{dp_{\text{lab}}}{dp_{\text{inc}}}, \tag{4.23}$$

Here the $\frac{dp_{lab}}{dp_{inc}}$ can be obtained by taking the derivative of Eq. 4.20 with respect to p_{inc}.

$$\frac{dp_{\text{lab}}}{dp_{\text{inc}}} = \gamma\left(1 + \frac{\beta p_{\text{inc}}}{\sqrt{m_0^2 + p_{\text{inc}}^2}}\right) \tag{4.24}$$

The calculated distributions provided do not take into account the resolution of the S800 CRDCs and the energy loss through the target. Therefore, the resolution was determined using the unreacted ^{106}Sn beam, which is convoluted with the eikonal predictions. These convoluted momentum distributions are compared with the experimental momentum distributions for the first excited state (see Sec. 5.3).

4.8 Cross Section Calculations

Cross section is the probability that an incident beam interacts with a target nucleus to populate a specific final configuration of the reaction residue. They provide insight into the nulcear wavefunction purity. If N_i is the number of incident ^{106}Sn beam particles on the target and N_f is the number of reaction products, then the reaction cross section σ is

defined as:

$$\sigma = \frac{N_f}{N_i} \frac{1}{d \times n}, \tag{4.25}$$

where d is the target thickness, and n is the number density.

$$n = \frac{\rho_m}{M} N_A \tag{4.26}$$

ρ_m is the mass density of the target, M is the molar mass and N_A is Avogadro's number.

For this work, the number of incoming beam particles was determined from the scaler counts of the OBJ timing scintillator located upstream of the target(N_{obj}). These counts were corrected for the OBJ scintillator detection efficiency ($\varepsilon_{\mathrm{real}}$) and for the "scaler deadtime" arising from multiple particles triggering the OBJ detector but being recorded as a single count ($\varepsilon_{\mathrm{pileup}}$). Therefore, N_i can be written as:

$$N_{\mathrm{i}} = \frac{N_{\mathrm{obj}}\ f_{\mathrm{p}}\ (1 - f_{\mathrm{loss}})}{\varepsilon_{\mathrm{real}}\ \varepsilon_{\mathrm{pileup}}}, \tag{4.27}$$

where f_{p} represents the beam purity as measured at the focal plane, which refers to the fraction of beam particles that are ^{106}Sn. The beam purity can be determined using data taken with no target in place and is obtained as 8.2(5)%. f_{loss} is the factor that accounts for the extra "loss" of beam-on-target particles, which represents the fraction of beam lost between the OBJ scintillator and the focal plane. This factor of around 64(2)% can be for any reasons, one of which we suspect to be beam particles, which pick up an electron going through the XFP scintillator and make it to OBJ but not to the focal plane.

The number of counts in the corresponding final state is calculated by:

$$N_{\mathrm{f}} = \frac{N_{\mathrm{res}}}{\varepsilon_{\mathrm{xfp+obj}}\ \varepsilon_{\mathrm{livetime}}\ f_{\mathrm{c}}}, \tag{4.28}$$

where N_{res} is the number of detected recoils at the focal plane for each state, $\varepsilon_{\mathrm{xfp+obj}}$ is the combined efficiency of OBJ and XFP scintillators, taken from event-by-event data and $\varepsilon_{\mathrm{livetime}}$ is the S800 DAQ livetime fraction. During this experiment, the XFP scintillator

degraded over time, hence the combined efficiency from OBJ and XFP scintillator was around $57(5)\%$ and $\varepsilon_{\text{livetime}}$ was $86(4)\%$. Another factor to be considered is the correction for charge state, f_c. After passing through the target, the reaction residue can capture electrons. The charge state is:

$$q = Z - N_e, \tag{4.29}$$

where Z is the atomic number and N_e is the number of bound electrons. Since the spectrometer transmission is optimized for fully stripped ions ($q = Z$), only a fraction of the produced residues are detected. The experimentally observed residue yield therefore represents only the fully stripped component of the total production. To obtain the true number of reaction products, the measured residue yield must be corrected by dividing the fully stripped fraction obtained from charge-state calculations using LISE++ [29] for the unreacted beam setting. We measured the correction factors for both charge state 0 and 1, and they are 0.66 and 0.35, respectively. The corresponding values from LISE++ are 0.71 and 0.26.

Chapter 5

Results and Discussion

The results of the analysis of the experimental data using the calibrations and corrections outlined in the preceding chapter are presented in this chapter. It involves recognizing the reaction fragments from the corrected particle identification spectra and the observed transitions in the gamma ray spectra. The momentum distribution for the ground and first excited states are extracted and discussed, along with the lifetime measurements for the first excited state obtained through comparisons between simulated and experimental γ-ray lineshapes. Finally, the calculated cross section are presented and compared with theoretical expectations.

5.1 Identification of reaction channels

5.1.1 Particle identification spectra

In the focal plane of the S800 spectrograph, the particles were detected on an event-by-event basis. The particles were identified using their energy loss and time-of-flight (TOF) measurements. The time-of-flight is related to the magnetic rigidity, and the energy loss of particles depends on their charge. The TOF from the E1-OBJ scintillators is plotted against the TOF from the E1-XFP scintillators to produce the secondary beam incoming histogram.

The incoming particle identification histogram shown in the Figure 5.1 is produced from the unreacted data run. The reacted secondary beam incoming PID is shown in the Figure 5.2.

The TOF versus TOF spectra provide a way to clearly identify the incoming beam particle. As shown in Figure 5.1, the beam contains isotopes of indium, cadmium, and silver as beam contaminants. After identifying the species in the secondary beam PID, a 2D "gate" can be placed around the specific isotone of interest. The incoming gate used for this work is shown in the Figure 5.1. Utilizing this gate, we can generate an energy loss (dE) vs time-of-flight (TOF) plot to observe all outgoing reaction products from that incoming beam (see Fig. 5.3b).

The E1-OBJ scintillators offer the timing information, while the ionization chamber provides the total energy loss (dE) information. The reaction products are not well resolved in this spectrum (Fig. 5.3b). Therefore, outgoing recoils could be uniquely identified on an event-by-event basis after corrections to time-of-flight, as described in the previous chapter (see Sec.4.4) are applied. These corrections to time-of-flight are needed to account for different flight paths of different reaction products. The residue PID, after applying the corrections is shown in Figure. 5.4, in which the reaction product ^{105}Sn isotope can be identified. As clearly shown in Figure 5.4, each of the different blobs represents a single isotope. While the vertical structure correlates to comparable A/q ratios, each nearly horizontal line represents a specific element. Each isotope can have gates drawn around it for data processing of the gamma rays detected by GRETINA and the ^{105}Sn gate used for further analysis is marked in the figure. Normally, the unreacted beam is blocked from reaching the focal plane. However, some components or charge states overlap with reaction products. Hence, to limit several strong features corresponding to the unreacted beam in the PID, the outgoing PID is constructed, requiring a coincident γ-ray, which considerably reduces the quantity of unreacted beam particles.

The coincidence requirement is just used to generate the plot in order to better visualize the position of the reaction products. This is useful for deciding proper gate location. However, it cannot be used to clean or filter the data for the rest of the study as reaction products are not always observed in conjunction with a γ-ray. In many circumstances,

the reaction populates the ground state and emits no γ-rays. The detection efficiency of the gamma ray detector alters the number of gamma rays detected. Here the separation between isotopes is improved after applying the energy and time-of-flight corrections to precisely separate each particle and its charge states.

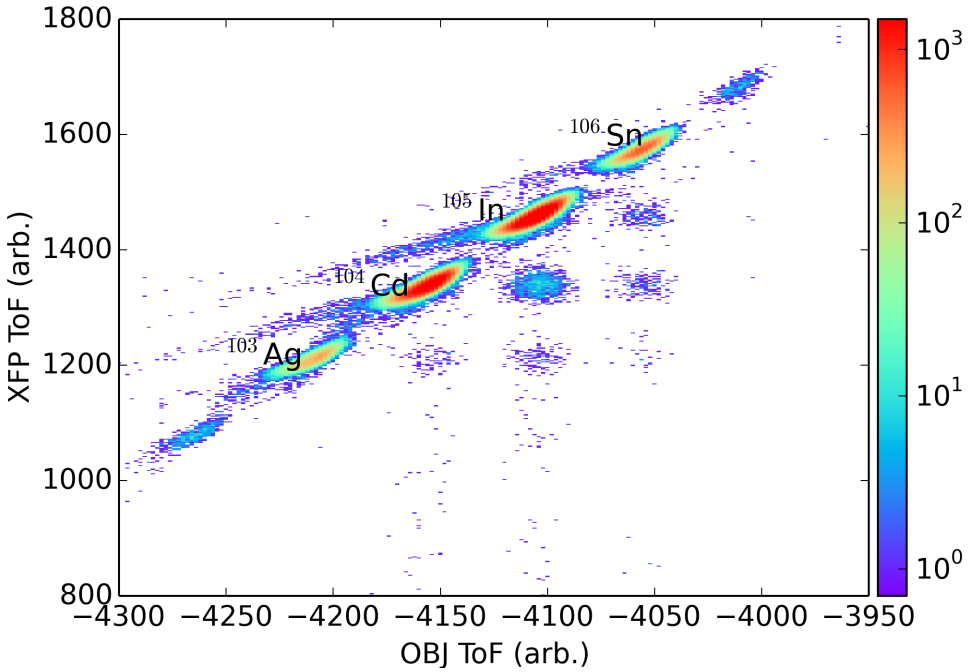


Figure 5.1: The unreacted beam incoming PID for one run. The TOF from the E1-OBJ scintillator is plotted against the TOF from the E1-XFP scintillator. The $N = 56$ isotones contaminants were present in the secondary incoming beam.

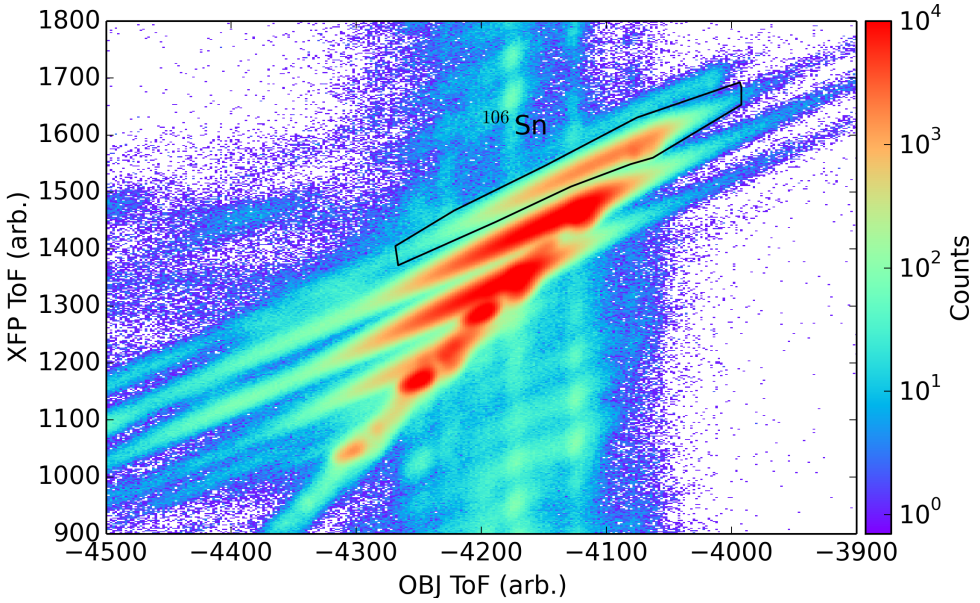
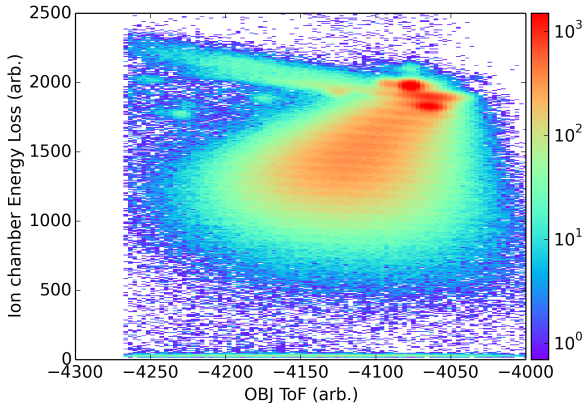
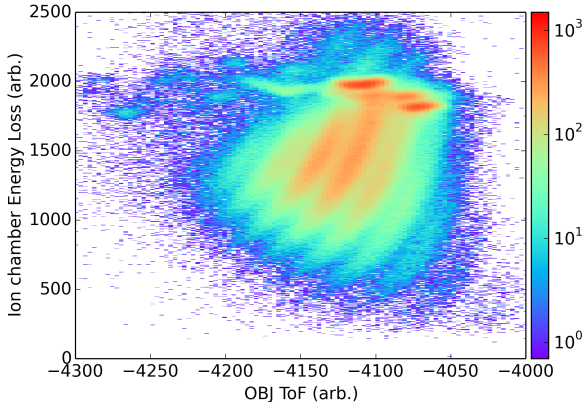


Figure 5.2: The reacted incoming PID from all the reaction settings data runs . The TOF from the E1-OBJ scintillators is plotted against the TOF from the E1-XFP scintillator. The ^{106}Sn incoming beam gate allows to select all the reaction products from that beam.



(a)



(b)

Figure 5.3: Energy loss in the S800 ionization chamber as a function of time-of-flight between the E1 and OBJ scintillators before corrections are applied. (a) shows the PID with no corrections and gamma gate applied, (b) shows the PID with the first-order ionization chamber and scintillator corrections.

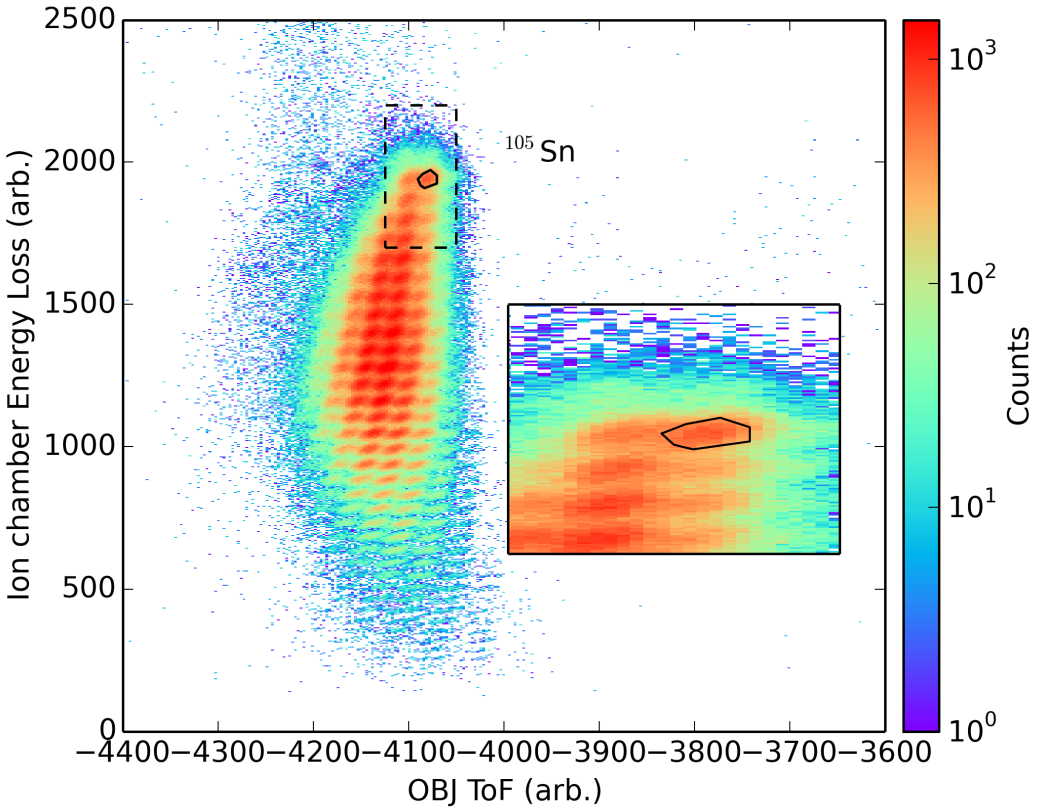


Figure 5.4: Energy loss in the S800 ionization chamber as a function of time-of-flight between the E1 and OBJ scintillator after applying calibrations and corrections to S800 focal plane detectors with a γ-ray coincidence requirement. Each of the different blobs represents a single isotope. While the vertical structure correlates to comparable A/q ratios, each nearly horizontal line represents a specific element. Each blob can have gates drawn around it for data processing of the gamma rays detected by GRETINA and ^{105}Sn gate used for further analysis is marked. The inset is zoomed into the tin isotopes.

5.2 γ-ray Spectra

By applying software gates to both incoming and outgoing Particle Identification (PID) spectra, it is possible to create γ-ray spectra that only show the γ-ray detected in coincidence with the chosen reaction channel. This spectrum is then compared to the known γ-ray transitions of the isotopes until a match is found. The Doppler-corrected spectrum following the one neutron knockout from the ^{106}Sn beam component is shown in Figure 5.5. The maximum likelihood method is used to fit the data using the response functions from the GEANT4-UCGretina simulations for the γ-ray transitions from the energy levels 200 keV, 1194 keV, 1394 keV and 1849 keV which corresponds to the $7/2^+$, $9/2^+$, $11/2^+$ and $13/2^+$ states, respectively, as shown in the level scheme in the Figure 4.10. These simulated γ-ray peaks are overlaid on the measured spectrum.

The γ-ray spectrum corresponding to events in which more than one γ-ray was detected ($\gamma_{\text{mul}} > 1$) and those with a single γ-ray was detected ($\gamma_{\text{mul}} = 1$) are shown separately in Figure 5.6. As discussed in Sec. 4.6.1, multiplicity-resolved spectra provide an effective method for distinguishing between background contributions and genuine nuclear γ-ray transitions, particularly in the low-energy region. This is evident in the $\gamma_{\text{mul}} > 1$ spectrum shown in Figure 5.6, where structures observed above the 200 keV transition in the $\gamma_{\text{mul}} > 1$ spectrum are not present in the $\gamma_{\text{mul}} = 1$ spectrum, indicating that the multiplicity gate is less sensitive to background as the peak-to-background ratio is high.

The γ-ray peaks measured at 200 keV, 655 keV and 1194 kev energies correspond to the transitions from states with spin and parity $7/2^+$ to $5/2^+$, $13/2^+$ to $9/2^+$ and $9/2^+$ to $5/2^+$, respectively, as illustrated in the level scheme shown in Figure 4.10. The 200 keV peak corresponds to the decay of the first excited state in ^{105}Sn, populated following the one-neutron knockout from the weakly bound valence neutrons, and other peaks from higher lying states in the residual nucleus. The nuclear shell model discussed in Sec. 2.1 gives a large energy gap between the $d_{5/2}$ and $g_{7/2}$ orbitals and the higher-lying $d_{3/2}, h_{11/2}, h_{9/2}$ neutron orbitals. This implies that the valence neutrons predominantly occupy the $d_{5/2}$ and $g_{7/2}$ orbitals. Thus, a simple one-neutron knockout reaction removing a weakly bound

valence neutron leads to the population of the lowest-lying states in ^{105}Sn. However, the measured γ-spectrum has peaks other than the 200 kev transition depopulating the first excited state. This indicates de-excitation from higher-lying states which suggests the removal of a neutron out of the ^{100}Sn core or a more complex reaction picture. There is a possibility that the higher lying states populated in this reaction are not simple one-neutron states. This is maybe not so surprising when we consider there are 50 neutrons in the core compared with 6 valence neutrons.

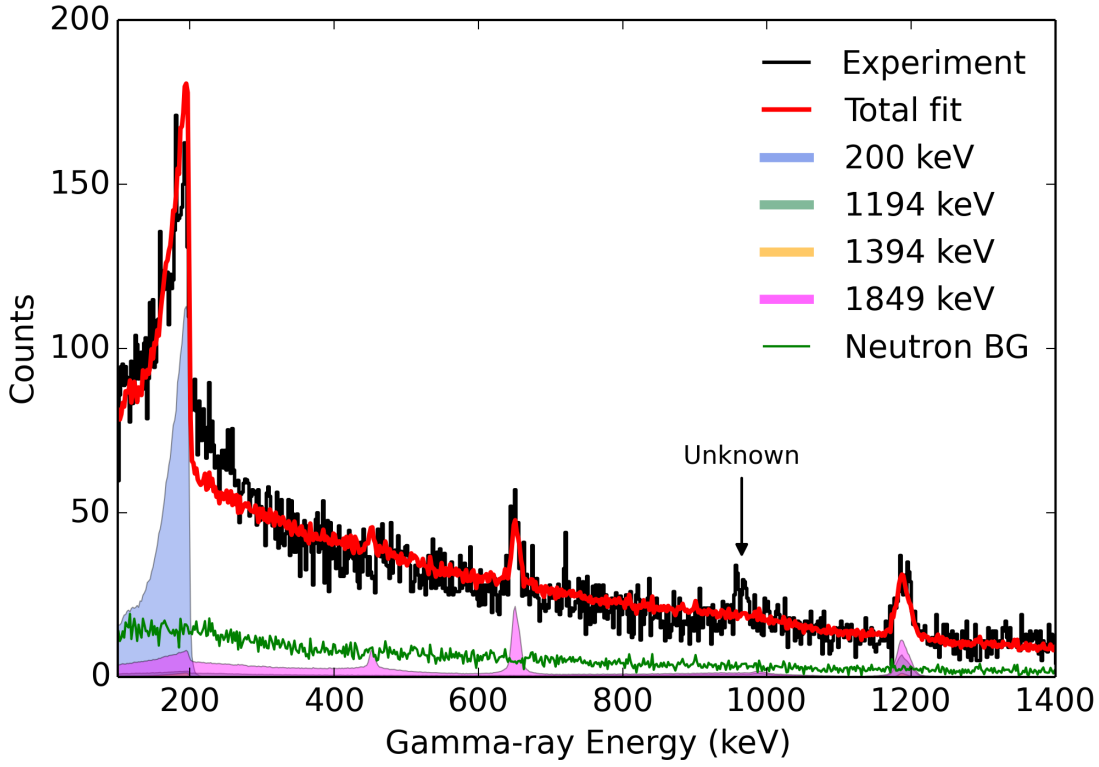


Figure 5.5: The Doppler-corrected gamma ray spectrum following the one-neutron knockout reaction on ^{106}Sn beam. Simulated spectra for states populated resulting the γ-ray transitions are plotted on the x-axis, with total fitting given as red line using the Maximum Likelihood method. The neutron background for the fitting is given as a green line. The fit also takes into account an exponential background.

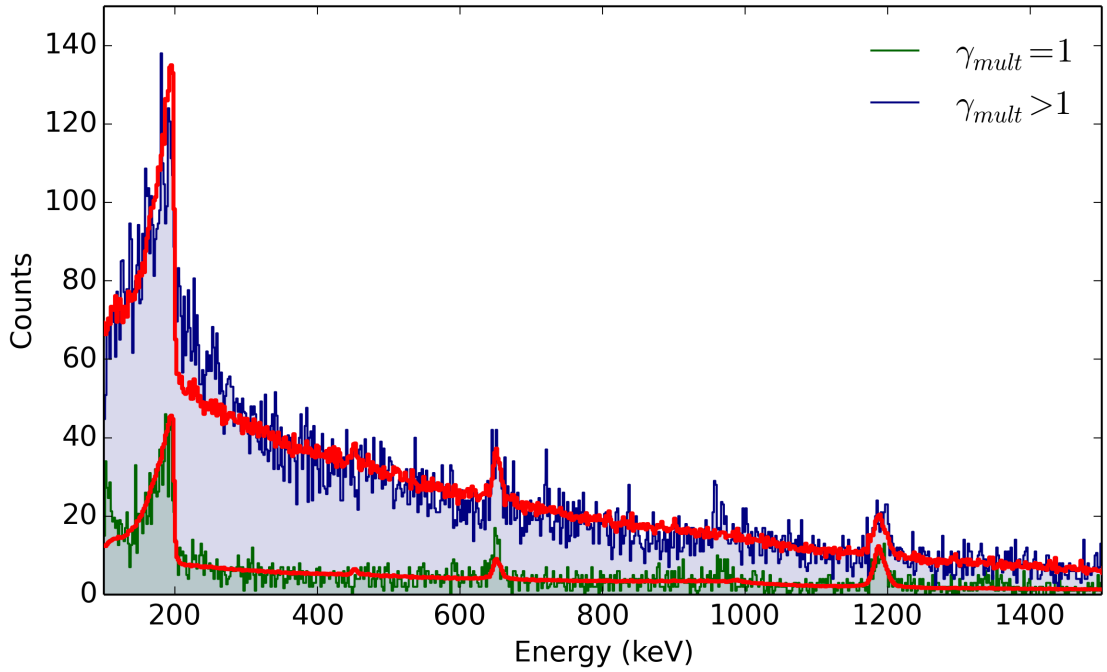


Figure 5.6: The spectra are separated into those where more than one γ-ray was detected ($\gamma_{\text{mul}} > 1$)(blue shaded region) and those where only one gamma ray was detected ($\gamma_{\text{mul}} = 1$)(green shaded region) and fitted using the UCGretina framework. The peak-to-background is much larger for $\gamma_{\text{mul}} = 1$, especially at low energies.

5.3 Lifetime and Spin assignments of first excited state

The study by G.Pasqualato et.al [11], measured the lifetime of the first excited state ($7/2^+$) in ^{105}Sn using the γ-γ-1p coincidence technique in conjuction with the Recoil Distance Doppler Shift (RDDS) method. They reported a lifetime of $\tau(7/2^+) = 0.61(3)$ ns, corresponding to a half-life value of 0.423(21) ns.

In the present work, the lifetime is extracted from the lineshape of the γ-ray peak at 200 keV using a minimum χ^2 fitting procedure, as described in Sec. 4.6.2. A velocity of $\beta = 0.3732$, determined using the procedure outlined in Sec. 4.5.1 is used for the Doppler correction. The analysis of the lifetime for the first excited state in the current work yields a value of τ = 720(190) ps corresponding to a half-life of 0.499(131) ns. The extracted lifetime of the $7/2^+$ state in this experiment agrees, within the uncertainties, with the previously mentioned value. The relatively large uncertainity in the extracted lifetime arises mainly due to the low statistics in the 200 keV transition, which reduces the sensitivity of the lineshape to variations in the lifetime.

The momentum distribution for the first excited state in the ^{105}Sn residue is obtained by reconstructing the momentum distribution in the energy region around the 200 keV peak in the γ-ray spectrum by following the procedure discussed in Sec. 4.7.1. The results of eikonal model reaction calculations (see Sec. 2.3, [32]), after convolution with an experimental resolution are overlaid and shown in Figure 5.7. The colored curves show the calculated distribution when assuming the one-neutron removal from a $2d_{5/2}$ orbital (green) and a $1g_{7/2}$ orbital (red). The χ^2 values are calculated for both the fits and are obtained as $\chi^2 = 9.54$ and 194 for l = 4 and l = 2 fits, respectively, with reduced χ^2 values as 1.36 and 27.72, respectively. Hence, for the first excited state transition, the l=4 scenario better represents the width of the momentum distribution, especially on the high momentum side, where the data are more reliable as the reaction is cleaner. When compared to the knockout calculations, the data reveal an excess of events results in a tail on the low momentum side where more dissipative, energy-sharing events occur due to the elastic scattering of the residue with the target, which has been shown to broaden the

momentum distribution [33][34]. Therefore comparisons are made to the central and high momentum distributions. The width of the peak is the important factor taken into account while comparing the experimental and theoretical momentum distributions. We conclude that the ^{105}Sn first excited state results from $g_{7/2}$ neutron removal. It can be confirmed after assigning spin to the ground state which is discussed in Section 5.4.

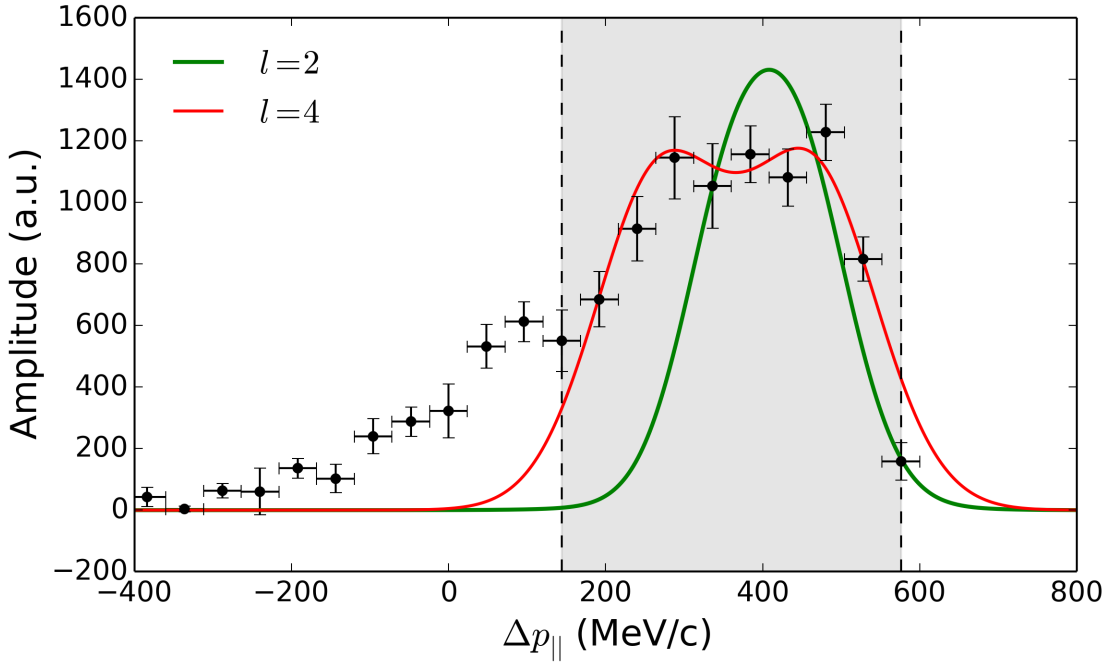


Figure 5.7: The momentum distribution of ^{105}Sn reaction residue in the first excited state compared with the eikonal model calculations for neutron removal from $l = 2$ (green), and $l = 4$ (red) orbitals. Data is fitted for the shaded region. The χ^2 value for both fit are $\chi^2 = 9.54$ and 194 for $l = 4$ and $l = 2$ fits, respectively. Hence $l = 4$ gives a good fit for the momentum distribution for the first excited state.

5.4 Momentum distribution for the ground state of ^{105}Sn

The exclusive momentum distribution for the ground state can be determined by subtracting the momentum distribution of all excited states from the total inclusive momentum distribution. Figure 5.8 illustrates the inclusive momentum distribution for the ^{105}Sn

residue and the momentum distributions of the lowest four excited states scaled with a factor from the simulated events for the $7/2^+$, $9/2^+$, $11/2^+$ and $13/2^+$ states populated in the reaction. The momentum distribution after the subtraction is shown in Figure 5.9. The calculation assuming knockout of a $d_{5/2}$ neutron provides a good fit to the experimental data for ^{106}Sn to the ground state of ^{105}Sn. In Figure 5.9, both $l = 2$ and $l = 4$ calculations are compared with the momentum distribution width, and the χ^2 values for the two fits are extracted as $\chi^2 = 5.03$ and 48.20 for $l = 2$ and $l = 4$ fits, respectively. The reduced χ^2 values calculated are 0.63 and 6.03, respectively for $l = 2$ and $l = 4$ fits. Hence, the $l = 2$ calculation provides a good fit, and the ground state of ^{105}Sn has been assigned a spin-parity of $5/2^+$. Therefore, the spin-parity for first excited state is confirmed to be $7/2^+$. These spin-parity assignments follow the trend for light tin isotopes as predicted by the shell model calculations discussed in Section 2.1 and are in agreement with the results from the study by Darby et al. [2] under either of the orbital orderings discussed in Section 1.1. Moreover, we have shown that the ground state momentum distribution can be reliably extracted using this method despite the large subtractions involved.

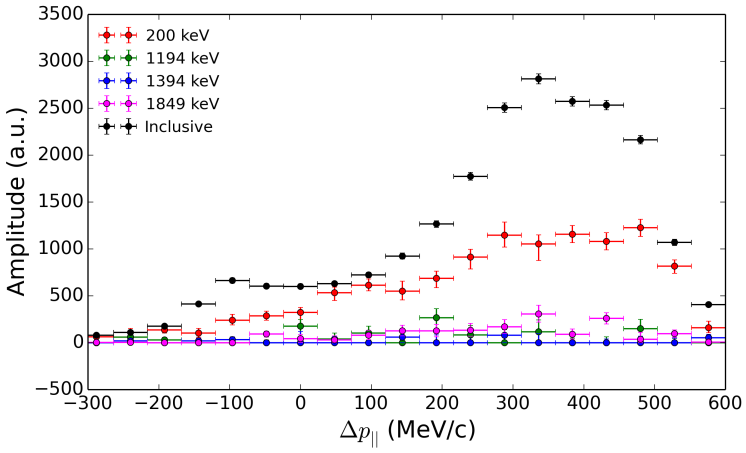


Figure 5.8: The inclusive momentum distribution for ^{105}Sn reaction residue (black points), with momentum distributions for the four lowest excited states scaled by the factor from simulated events.

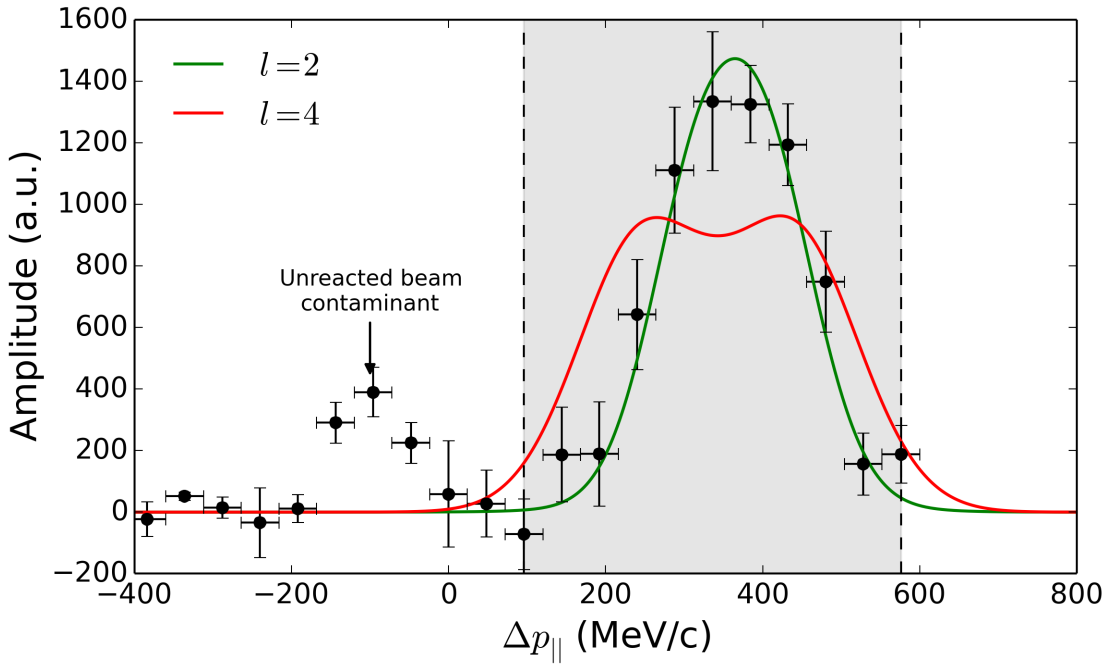


Figure 5.9: The exclusive momentum distribution for the ground state of the ^{105}Sn reaction residue is obtained by subtracting the momentum distributions of all dominant bound excited states from the inclusive momentum distribution. The data is overlaid with eikonal model reaction calculations assuming $l = 2$ (red) and $l = 4$ (green) knockout. The χ^2 value for both fit are $\chi^2 = 5.03$ and 48.20 for $l = 2$ and $l = 4$ fits, respectively. Hence $l = 2$ gives a good fit for the momentum distribution for the ground state. The structure seen in the lower momentum region is from the unreacted beam contaminants and hence not taken into account in any calculations.

5.5 Cross Section

The inclusive cross-section measurements for one-neutron removal from ^{106}Sn, along with the partial cross sections to the low-lying states in ^{105}Sn are summarized in Table 5.2. These experimental results are compared with theoretical predictions obtained from the calculations using the eikonal reaction model as described in Section 2.3, and shell-model structure inputs. Shell model calculations were performed using the $\nu(d_{5/2}, g_{7/2}, d_{3/2}, h_{11/2}, s_{1/2})$ model space using two variants of the jj55pna interaction [35]. The first variant, "jj55pna", adjusted the single particle energy separation such that $\Delta\varepsilon_{sp} = \mathrm{SPE}(g_{7/2}) - \mathrm{SPE}(d_{5/2}) =$ 172 keV. The second "jj55pna(inv)" inverted the ordering of the $g_{7/2}$ and $d_{5/2}$ orbitals, $\Delta\varepsilon_{sp} = -172$ keV. These calculations qualitatively reproduce those presented in Ref. [2].

The results from these calculations are shown in Table 5.1.

For knockout leading to the $5/2^+$ ground state in ^{105}Sn, the measured cross section is systematically smaller than the calculations from both models, and for knockout to the $7/2^+$ first excited state the measured value is larger than both theory values. A dominant source of uncertainty, which may not be accurately quantified, relates to the normalization factor and efficiencies in equations for N_i and N_f given in equations 4.28 and 4.28, respectively. At present the systematic uncertainty resulting from these factors amounts to $\approx 15\%$, which is included in the values in Table 5.2. In particular, the transmission losses of the beam of interest (^{106}Sn), and the contaminants between the OBJ scintillator and the focal plane may not be well understood. Additionally, variations in different detector efficiencies, including the OBJ and XFP scintillator efficiencies, may play a dominant role.

Table 5.1: Summary table of shell-model spectroscopic factor (C^2S) calculations from ^{106}Sn beam. The experimental calculations for $\mathrm{S}(J^\pi) = (C^2S/(2J+1))$ are compared with the calculations using the jj55pna model space. For jj555pna standard model space $\Delta\varepsilon_{s.p} =$ 172keV and for jj55pna(inv) model $\Delta\varepsilon_{s.p} = -172$keV.

J^π	C^2S_{exp}	$\mathrm{S}(J^\pi)_{\mathrm{exp}}$	$S(J^\pi)_{\mathrm{jj55pna}}$	$S(J^\pi)_{\mathrm{jj55pna(inv)}}$
$5/2^+$	1.2	0.20	0.58	0.41
$7/2^+$	4.0	0.50	0.39	0.42

Table 5.2: Summary table of inclusive and exclusive neutron removal cross sections from ^{106}Sn beam from both experimental and theoretical calculations. The inclusive cross section is the total cross section of the reaction, regardless of the knockout channel.

Final state	σ_{exp} (mb)	$\sigma_{jj55pna}$ (mb)	$\sigma_{jj55pna(inv)}$ (mb)
Ground state ($5/2^+$)	11.5(19)	33.2	23.7
First excited ($7/2^+$)	18.4(27)	10.9	15.4
Inclusive	36(5)		

However, the relative cross section $\sigma(7/2^+)/\sigma(5/2^+)$ is much less sensitive to uncertainties in the normalization. The experimental relative cross section is compared to the results of the eikonal model, taking spectroscopic factors from the two jj55pna calculations in is given in Table 5.3. The experimental ratio for $\sigma(7/2^+)/\sigma(5/2^+)$ = 1.61(14) is significantly larger than the ratios from both interactions. This indicates that the $g_{7/2}$ has more strength relative to the $d_{5/2}$. When compared to shell model expectations, this value is larger, which can be due to the possibility of unobserved feeding into the $7/2^+$ state and hence the excess of strength for this state.

Table 5.3: Summary of relative cross sections calculated ($\sigma(7/2^+)/\sigma(5/2^+)$) from the experiment and the two model spaces: jj55pna and jj55pna(inv).

Source	$\sigma(7/2^+)/\sigma(5/2^+)$
Exp.	1.61(14)
jj55pna	0.33
jj55pna(inv)	0.65

Chapter 6

Conclusion

The study was motivated by the need to probe the nuclear structure in the regions close to the doubly magic ^{100}Sn. An experiment to study the structure of ^{105}Sn was conducted in December 2022 at the Facility for Rare Isotope Beams (FRIB) at Michigan State University. The experiment was the one-neutron knockout reaction, using a ^{106}Sn beam on a ^{9}Be target, denoted by ^{9}Be(^{106}Sn, ^{105}Sn+γ)X. A primary beam of ^{124}Xe was accelerated in the driver linac and fragmented on a ^{9}Be target, which produced a secondary beam of ^{106}Sn, separated using the Advanced Rare Isotope Separator (ARIS). This beam reacts with a secondary ^{9}Be target in the S800 spectrograph target chamber surrounded by the GRETINA detector, which measures the γ-rays in coincidence with the neutron knockout reaction, allowing us to differentiate between the ground and first excited state knockout channels. The reaction residues were identified event-by-event using the time-of-flight between two plastic timing scintillators and the energy loss measured in the S800 focal plane ionization chamber (IC). The Cathode Readout Drift Chambers (CRDC) measured the particle positions and angles in the focal plane. These position and angle information combined with trajectory reconstruction through the spectrograph using the COSY INFINITY code, is used to reconstruct the longitudinal momentum distributions of the reaction residue at the target position. The width of the momentum distributions was used to extract the orbital angular momentum l quantum number of the removed nucleon so that the spin and parity of the

state can be assigned by comparing with the theoretical distribution calculated from the Spectator Core Eikonal Model. This concluded that the ground state of ^{105}Sn has a spin-parity of $J^{\pi} = 5/2^{+}$ and the first excited state has $J^{\pi} = 7/2^{+}$.

6.1 Future outlook

Knockout measurements on light tin isotopes are planned to continue, with emphasis on the one-neutron knockout from ^{102}Sn. These measurements will make J^{π} assignments for the ground and first excited states in ^{101}Sn, which remain key benchmarks for testing shell-model predictions near the double magic ^{100}Sn. The present experiment serves as an important step in establishing the feasibility of these future one-neutron knockout studies, including validating the experimental setup, reaction selectivity, and analysis techniques required for precise measurements.

In addition to the ^{106}Sn beam used in the experiment, one-neutron knockout reactions were performed on the ^{104}Sn beam to investigate the structure of ^{103}Sn. The experiment was not successful due to the low purity of beam and insufficient statistics, and a remeasurement is planned. These studies will contribute to understanding the degree of fragmentation of spectroscopic strength and the role of configuration mixing in nuclei near ^{100}Sn.

Bibliography

[1] D. Seweryniak, M. P. Carpenter, S. Gros, A. A. Hecht, N. Hoteling, R. V. F. Janssens, T. L. Khoo, T. Lauritsen, C. J. Lister, G. Lotay, D. Peterson, A. P. Robinson, W. B. Walters, X. Wang, P. J. Woods, and S. Zhu. Single-neutron states in ^{101}Sn. *Phys. Rev. Lett.*, 99:022504, Jul 2007. x, 2, 3, 5

[2] I. G. Darby, R. K. Grzywacz, J. C. Batchelder, C. R. Bingham, L. Cartegni, C. J. Gross, M. Hjorth-Jensen, D. T. Joss, S. N. Liddick, W. Nazarewicz, S. Padgett, R. D. Page, T. Papenbrock, M. M. Rajabali, J. Rotureau, and K. P. Rykaczewski. Orbital dependent nucleonic pairing in the lightest known isotopes of tin. *Phys. Rev. Lett.*, 105:162502, Oct 2010. x, 2, 6, 7, 73, 75

[3] G. Cerizza, A. Ayres, K. L. Jones, R. Grzywacz, A. Bey, C. Bingham, L. Cartegni, D. Miller, S. Padgett, T. Baugher, D. Bazin, J. S. Berryman, A. Gade, S. McDaniel, A. Ratkiewicz, A. Shore, S. R. Stroberg, D. Weisshaar, K. Wimmer, R. Winkler, S. D. Pain, K. Y. Chae, J. A. Cizewski, M. E. Howard, and J. A. Tostevin. Structure of ^{107}Sn studied through single-neutron knockout reactions. *Phys. Rev. C*, 93:021601, Feb 2016. x, 3, 8

[4] R. F. Casten. *Nuclear Structure from a Simple Perspective*. Oxford University Press, 2000. x, 12

[5] Alexandra Gade and Thomas Glasmacher. In-beam nuclear spectroscopy of bound states with fast exotic ion beams. *Progress in Particle and Nuclear Physics*, 60(1):161–224, 2008. xi, 13, 15

[6] J. A. Tostevin, D. Bazin, B. A. Brown, T. Glasmacher, P. G. Hansen, V. Maddalena, A. Navin, and B. M. Sherrill. Single-neutron removal reactions from ^{15}C and ^{11}Be: Deviations from the eikonal approximation. *Phys. Rev. C*, 66:024607, Aug 2002. xi, 18

[7] M. Portillo, B.M. Sherrill, Y. Choi, M. Cortesi, K. Fukushima, M. Hausmann, E. Kwan, S. Lidia, P.N. Ostroumov, R. Ringle, M.K. Smith, M. Steiner, O.B. Tarasov, A.C.C. Villari, and T. Zhang. Commissioning of the advanced rare isotope separator aris at frib. *Nuclear Instruments and Methods in Physics Research Section B: Beam Interactions with Materials and Atoms*, 540:151–157, 2023. xi, 20

[8] M. Hausmann, A.M. Aaron, A.M. Amthor, M. Avilov, L. Bandura, R. Bennett, G. Bollen, T. Borden, T.W. Burgess, S.S. Chouhan, V.B. Graves, W. Mittig, D.J. Morrissey, F. Pellemoine, M. Portillo, R.M. Ronningen, M. Schein, B.M. Sherrill, and A. Zeller. Design of the advanced rare isotope separator aris at frib. *Nuclear Instruments and Methods in Physics Research Section B: Beam Interactions with Materials and Atoms*, 317:349–353, 2013. XVIth International Conference on ElectroMagnetic Isotope Separators and Techniques Related to their Applications, December 2–7, 2012 at Matsue, Japan. xi, 22, 23

[9] D. Bazin, J.A. Caggiano, B.M. Sherrill, J. Yurkon, and A. Zeller. The s800 spectrograph. *Nuclear Instruments and Methods in Physics Research Section B: Beam Interactions with Materials and Atoms*, 204:629–633, 2003. 14th International Conference on Electromagnetic Isotope Separators and Techniques Related to their Applications. xi, 23, 24

[10] National Nuclear Data Center. Evaluated nuclear structure data file (ensdf) dataset retrieval, 2024. Accessed: 10 Mar 2026. xiii, 47

[11] G. Pasqualato, A. Gottardo, D. Mengoni, A. Goasduff, J.J. Valiente-Dobón, F. Nowacki, S. Péru, N. Pillet, G. de Angelis, S.D. Bakes, T. Bayram, D. Bazzacco, G. Benzoni, D. Brugnara, M. Cicerchia, P. Colovic, M.L. Cortés, A. Gadea,

F. Galtarossa, M. Górska, A. Gozzelino, E. Gregor, N. Hubbard, A. Illana, M. Jurado, S.M. Lenzi, G. Mantovani, T. Marchi, R. Menegazzo, A. Montaner-Pizá, D.R. Napoli, F. Recchia, M. Siciliano, D. Testov, S. Szilner, and I. Zanon. An alternative viewpoint on the nuclear structure towards 100sn: Lifetime measurements in 105sn. *Physics Letters B*, 845:138148, 2023. xiv, 56, 71

[12] R. K. Wallace and S. E. Woosley. Explosive hydrogen burning. , 45:389–420, February 1981. 1

[13] Morten Hjorth-Jensen, Thomas T.S. Kuo, and Eivind Osnes. Realistic effective interactions for nuclear systems. *Physics Reports*, 261(3):125–270, 1995. 3

[14] J A Tostevin. Core excitation in halo nucleus break-up. *Journal of Physics G: Nuclear and Particle Physics*, 25(4):735, apr 1999. 4, 58

[15] Maria Goeppert Mayer and J. Hans D. Jensen. *Elementary Theory of Nuclear Shell Structure*. Wiley, New York, 1st edition, 1955. 12. 9, 10

[16] O. Sorlin and M.-G. Porquet. Nuclear magic numbers: New features far from stability. *Progress in Particle and Nuclear Physics*, 61(2):602–673, October 2008. 14

[17] A. Gade, D. Bazin, B. A. Brown, C. M Campbell, J. A. Church, D. C. Dinca, J. Enders, T. Glasmacher, P. G. Hansen, Z. Hu, K. W. Kemper, W. F. Mueller, H. Olliver, B. C. Perry, L. A. Riley, B. T. Roeder, B. M. Sherrill, J. R. Terry, J. A. Tostevin, and K. L. Yurkewicz. One-neutron knockout reactions on proton-rich nuclei with $n = 16$. *Phys. Rev. C*, 69:034311, Mar 2004. 15

[18] J.A. Tostevin. Single-nucleon knockout reactions at fragmentation beam energies. *Nuclear Physics A*, 682(1):320–331, 2001. 16

[19] M.S. Hussein and K.W. McVoy. Inclusive projectile fragmentation in the spectator model. *Nuclear Physics A*, 445(1):124–139, 1985. 16

[20] P. G. Hansen and J. A. Tostevin. Direct reactions with exotic nuclei. *Annual Review of Nuclear and Particle Science*, 53:219–261, 2003. 16

[21] J. A. Tostevin and A. Gade. Systematics of intermediate-energy single-nucleon removal cross sections. *Phys. Rev. C*, 90:057602, Nov 2014. 16

[22] Xiaoyu Wu, Chris Compton, Marc Doleans, Walter Hartung, Don Lawton, Felix Marti, Richard York, and Qiang Zhao. The MSU-Proposed Superconducting Driver Linac for the FRIB Project. In *Particle Accelerator Conference (PAC 09)*, page FR5REP073, 2010. 21

[23] R Madendorp, T Maruta, Jerry Nolen, P Ostroumov, Jyunlin Wei, Qs Zhao, D Chojnowski, Claude Reed, J Specht, Takuji Kanemura, M. LaVere, F. Marti, Nathan Bultman, Yoichi Momozaki, and Alexander Plastun. Rd of liquid lithium stripper at frib*. 09 2022. 21

[24] K. Makino and M. Berz. COSY INFINITY version 8. *Nucl. Instrum. Meth. A*, 427:338–343, 1999. 30, 55

[25] S. Paschalis, I.Y. Lee, A.O. Macchiavelli, C.M. Campbell, M. Cromaz, S. Gros, J. Pavan, J. Qian, R.M. Clark, H.L. Crawford, D. Doering, P. Fallon, C. Lionberger, T. Loew, M. Petri, T. Stezelberger, S. Zimmermann, D.C. Radford, K. Lagergren, D. Weisshaar, R. Winkler, T. Glasmacher, J.T. Anderson, and C.W. Beausang. The performance of the gamma-ray energy tracking in-beam nuclear array gretina. *Nuclear Instruments and Methods in Physics Research Section A: Accelerators, Spectrometers, Detectors and Associated Equipment*, 709:44–55, 2013. 32

[26] GRETINA Collaboration. Gretina gamma-ray tracking array, 2024. 32

[27] L.A. Riley, D. Weisshaar, H.L. Crawford, M.L. Agiorgousis, C.M. Campbell, M. Cromaz, P. Fallon, A. Gade, S.D. Gregory, E.B. Haldeman, L.R. Jarvis, E.D. Lawson-John, B. Roberts, B.V. Sadler, and C.G. Stine. Ucgretina geant4 simulation of the gretina gamma-ray energy tracking array. *Nuclear Instruments and Methods in*

Physics Research Section A: Accelerators, Spectrometers, Detectors and Associated Equipment, 1003:165305, 2021. 50

[28] S. Agostinelli, J. Allison, K. Amako, J. Apostolakis, H. Araujo, P. Arce, M. Asai, D. Axen, S. Banerjee, G. Barrand, F. Behner, L. Bellagamba, J. Boudreau, L. Broglia, A. Brunengo, H. Burkhardt, S. Chauvie, J. Chuma, R. Chytracek, G. Cooperman, G. Cosmo, P. Degtyarenko, A. Dell'Acqua, G. Depaola, D. Dietrich, R. Enami, A. Feliciello, C. Ferguson, H. Fesefeldt, G. Folger, F. Foppiano, A. Forti, S. Garelli, S. Giani, R. Giannitrapani, D. Gibin, J.J. Gómez Cadenas, I. González, G. Gracia Abril, G. Greeniaus, W. Greiner, V. Grichine, A. Grossheim, S. Guatelli, P. Gumplinger, R. Hamatsu, K. Hashimoto, H. Hasui, A. Heikkinen, A. Howard, V. Ivanchenko, A. Johnson, F.W. Jones, J. Kallenbach, N. Kanaya, M. Kawabata, Y. Kawabata, M. Kawaguti, S. Kelner, P. Kent, A. Kimura, T. Kodama, R. Kokoulin, M. Kossov, H. Kurashige, E. Lamanna, T. Lampén, V. Lara, V. Lefebure, F. Lei, M. Liendl, W. Lockman, F. Longo, S. Magni, M. Maire, E. Medernach, K. Minamimoto, P. Mora de Freitas, Y. Morita, K. Murakami, M. Nagamatu, R. Nartallo, P. Nieminen, T. Nishimura, K. Ohtsubo, M. Okamura, S. O'Neale, Y. Oohata, K. Paech, J. Perl, A. Pfeiffer, M.G. Pia, F. Ranjard, A. Rybin, S. Sadilov, E. Di Salvo, G. Santin, T. Sasaki, N. Savvas, Y. Sawada, S. Scherer, S. Sei, V. Sirotenko, D. Smith, N. Starkov, H. Stoecker, J. Sulkimo, M. Takahata, S. Tanaka, E. Tcherniaev, E. Safai Tehrani, M. Tropeano, P. Truscott, H. Uno, L. Urban, P. Urban, M. Verderi, A. Walkden, W. Wander, H. Weber, J.P. Wellisch, T. Wenaus, D.C. Williams, D. Wright, T. Yamada, H. Yoshida, and D. Zschiesche. Geant4—a simulation toolkit. *Nuclear Instruments and Methods in Physics Research Section A: Accelerators, Spectrometers, Detectors and Associated Equipment*, 506(3):250–303, 2003. 50

[29] LISE++ Development Team. Lise++ utilities, 2025. 50, 61

[30] N. Belmakier. Fitgretina, n.d. GitHub repository. 52

[31] M. Berz, K. Joh, J. A. Nolen, B. M. Sherrill, and A. F. Zeller. Reconstructive correction of aberrations in nuclear particle spectrographs. *Phys. Rev. C*, 47:537–544, Feb 1993. 55

[32] J. A. Tostevin, 2025. Private communication. 71

[33] S. R. Stroberg, A. Gade, J. A. Tostevin, V. M. Bader, T. Baugher, D. Bazin, J. S. Berryman, B. A. Brown, C. M. Campbell, K. W. Kemper, C. Langer, E. Lunderberg, A. Lemasson, S. Noji, F. Recchia, C. Walz, D. Weisshaar, and S. J. Williams. Single-particle structure of silicon isotopes approaching ^{42}Si. *Phys. Rev. C*, 90:034301, Sep 2014. 72

[34] C. A. Bertulani and P. G. Hansen. Momentum distributions in stripping reactions of radioactive projectiles at intermediate energies. *Phys. Rev. C*, 70:034609, Sep 2004. 72

[35] B. A. Brown, N. J. Stone, J. R. Stone, I. S. Towner, and M. Hjorth-Jensen. Magnetic moments of the 2_1^+ states around ^{132}Sn. *Phys. Rev. C*, 71:044317, Apr 2005. 75

Vita

Anna Peter is from Kerala, India. She completed her Bachelor of Science and Master of Science in Physics from Mahatma Gandhi University, Kottayam, in Kerala. She also completed her Bachelor of Education from Mahatma Gandhi University in 2020. She later joined the University of Tennessee, Knoxville, in 2021 to pursue graduate studies and started her research in the field of nuclear physics.